







Unidirectional and combined transitional flow bedforms: Controls on process and distribution in submarine slope settings

WILLIAM J. TAYLOR* , DAVID M. HODGSON* , JEFF PEAKALL* ,
IAN A. KANE† , EMMA A. MORRIS‡¹  and STEPHEN S. FLINT† 

*School of Earth and Environment, University of Leeds, Leeds LS2 9JT, UK (E-mail: eewjt@leeds.ac.uk)

†Department of Earth and Environmental Sciences, University of Manchester, Manchester M13 9PL, UK

‡Department of Earth, Ocean and Ecological Sciences, University of Liverpool, Liverpool L69 3GP, UK

Associate Editor – Lawrence Amy

ABSTRACT

Mixed grain-size bedforms comprise alternating sand-rich and poorly sorted mud-rich laminae and bands. These bedforms have been identified in distal submarine settings formed underneath unidirectional flows. This study documents mixed grain-size bedforms in a proximal submarine slope setting formed beneath both unidirectional and combined flows. Core and outcrop data with well-constrained palaeogeographical context are used to describe two types of mixed grain-size bedform. Type A bedforms comprise mud-rich current ripples and low-amplitude bed-waves with alternating concave and planar sandstone–mudstone foresets that pass into mud-rich troughs, and aggradational sinusoidal laminasets. Type B bedforms consist of sandstone–mudstone laminasets that comprise rounded, biconvex ripples with sigmoidal-shaped foresets and swale and hummock-like laminasets and banded sets. These bedforms occur in channel-margin, internal-levée and external-levée, intraslope and disconnected lobe environments, and represent 27 to 63% by stratigraphic thickness of the studied successions. They are interpreted as deposits of clay-rich transitional flows, whose depositional style is governed by the balance of cohesive and turbulent forces, and the rate of flow deceleration. Type B bedforms are further interpreted as combined transitional flow deposits, resulting from flow deflection and ponding processes by seabed topography. Upward and lateral transitions between different bedforms create distinct bedform sequences, demonstrating progressive spatio-temporal transformations in flow properties and their topographic interactions. By using a well-constrained palaeogeographical setting, mixed grain-size bedforms are shown to be situated close to sites of erosion into muddy substrates, abrupt losses in confinement, and/or changes in slope gradient. These bedforms demonstrate that flow transformation and transitional flow behaviour are not restricted to distal submarine settings. Furthermore, mixed grain-size bedforms are not a diagnostic criterion for bottom currents, because such flows cannot account for the high mud content in laminasets, or the interlamination of sand and mud.

Keywords Bedforms, cohesion, combined flows, mixed grain size, submarine slopes, topography, transitional flows.

¹Present address: Department of Geology and Geophysics, University of Utah, Salt Lake City, UT 84112-0102, USA

INTRODUCTION

Bedforms are rhythmic features formed by the entrainment and deposition of material at the interface between a flowing fluid and a moveable bed (e.g. Allen, 1968; Wilson, 1972; Southard, 1991; Baas *et al.*, 2016). The understanding of bedforms is important for the reconstruction of flow processes in ancient sedimentary systems and to support interpretations of the spatio-temporal evolution of depositional environments (e.g. Sorby, 1908; Harms *et al.*, 1975; McLean & Smith, 1979; Allen, 1982; Bridge & Best, 1988; Southard & Boguchwal, 1990; Kneller, 1995). In deep-marine settings, bedforms are typically formed by sediment gravity flows (SGFs) (e.g. Bouma, 1962; Lowe, 1982; Talling *et al.*, 2012; Hage *et al.*, 2018), contour currents (e.g. Stow & Lovell, 1979; Rebesco *et al.*, 2014; Fuhrmann *et al.*, 2022) or internal tides (e.g. Gardner, 1989; Maier *et al.*, 2019), that transport and redistribute particulates from continents to the deep ocean.

Most SGFs contain clay particles that aggregate to form floccules and gels (Winterwerp & van Kesteren, 2004). These increase cohesive forces during flow deceleration, and thus can enhance or suppress turbulence (Baas & Best, 2002; Sumner *et al.*, 2008; Baas *et al.*, 2009, 2011). The addition of small volumes of clay to a turbulent, sand-laden flow can produce distinctive mixed grain-size bedforms, which this study defines as bedforms comprising alternations of sand-rich and poorly sorted mud-rich laminae and bands. Mixed grain-size bedforms can have different shapes, sizes and textures when compared with bedforms associated with non-cohesive flows (Baas *et al.*, 2011, 2013; Schindler *et al.*, 2015). The experimental work of Baas *et al.* (2016) showed how mixed grain-size sedimentary structures were produced by cohesive flows composed of clay, silt and sand particles, which comprised large current ripples and low-amplitude bed-waves (LABWs). These mixed grain-size bedforms were controlled by the balance of cohesive and turbulent forces in the flow, and clay type (Baas *et al.*, 2016; Baker *et al.*, 2017). Such bedforms can also vary in their geometry and texture during rapid deceleration of a mud-rich cohesive flow, as shown by the analysis of a single climbing ripple (Baas *et al.*, 2021a).

These studies of clay-rich flows demonstrated that existing models, which interpret deposits as products of flows where cohesive forces were considered to have minimal effect on deposition, are not appropriate to interpret mixed grain-size bedforms, including low-density turbidites

(Bouma, 1962), high-density turbidites (Lowe, 1982) and near-bed grain flow deposits (Mutti, 1992). These models do not describe facies divisions with heterolithic sedimentary structures. Recent models describe longitudinal and/or vertical segregation of fine-grained cohesive particles, which lead to flow transformation via turbulence suppression and the generation of laminar plug flows (Haughton *et al.*, 2009; Baas *et al.*, 2011, 2021b). These processes preferentially lead to the deposition of hybrid event beds (HEBs) at the fringes of fine-grained submarine fan systems (Talling *et al.*, 2004; Hodgson, 2009; Kane & Pontén, 2012; Kane *et al.*, 2017; Pierce *et al.*, 2018). Furthermore, Stevenson *et al.* (2020) described sandstone–mudstone banding and discussed how the juxtaposition of hydrodynamically different grain sizes further contradicts the established models of cleaner-sand bedform development. Such structures were likely formed within, or at the boundaries of, the upper stage plane bed regime via tractional reworking beneath mud-rich transitional flows (Stevenson *et al.*, 2020). In the ancient rock record, bedforms attributed to cohesive, transitional flows have been documented in lobe fringe and distal lobe fringe environments (Baker & Baas, 2020; Privat *et al.*, 2021; Baas *et al.*, 2021b; Łapcik, 2023), channel-lobe transition zones (Brooks *et al.*, 2022) and lacustrine environments (Dou *et al.*, 2021; Baas *et al.*, 2021a). In contrast, the texture, geometry and spatio-temporal distribution of mixed grain-size bedforms have not been documented in proximal locations, such as submarine slope successions. This is surprising, given the availability of large quantities of mud that can be entrained, and the numerous locations of abrupt losses in flow confinement, which should mean that submarine slope systems are conducive to flow transformations through changes in the balance of cohesive and turbulent forces.

At present, transitional flow bedforms are considered to form under unidirectional currents. However, bedforms with flow structures attributed to the interaction of SGFs with topography are increasingly identified (e.g. Tinterri, 2011; Tinterri *et al.*, 2022). These bedforms are documented in basin plain environments (Pickering & Hiscott, 1985; Haughton, 1994; Tinterri & Muzzi Magalhaes, 2011; Bell *et al.*, 2018; Tinterri *et al.*, 2022), channel-lobe transition zones (Hofstra *et al.*, 2018) and intraslope basins (Gallicchio *et al.*, 2023), where they are characterized by convex-up structures and small-scale hummock-like cross-stratification that differ markedly from

the deposits of fully unidirectional flows and traditional hummocky cross-stratification (HCS) (Harms *et al.*, 1975; Tinterri, 2011; Hofstra *et al.*, 2018; Tinterri *et al.*, 2022). Areas where flows interact with mud-prone intrabasinal slopes may be prime locations for flow transformations and the development of mixed grain-size bedforms, but this association has not been proven.

This study aims to document a range of mixed grain-size bedforms across several well-constrained, topographically complex mid to lower slope environments, using core and outcrop data from the Permian Fort Brown and Laingsburg formations, South Africa. The objectives of this study were to: (i) identify, describe and classify distinctive laminasets that form mixed grain-size bedforms, based on their shape, size, texture and internal stratification; (ii) place constraints on the spatial and stratigraphic distribution of mixed grain-size bedforms; and (iii) interpret and discuss the formational processes that generate bedform types. Based on the results, a model that links the formative flow processes of mixed grain-size bedforms with their stratigraphic and spatial distribution in submarine slope settings is presented. This work provides an effective tool to aid process understanding and prediction of proximal locations such as submarine slope settings.

THE KAROO BASIN

The early subsidence of the Karoo Basin during the Permian is attributed to dynamic topography (mantle flow) during subduction (Pysklywec & Mitrovica, 1999), before a transition to a retro-arc foreland basin stage during the Triassic (Tankard *et al.*, 2009, 2012; Blewett & Phillips, 2016). The late Carboniferous to Triassic basin fill (Karoo Supergroup) is approximately 8 km thick, and encompasses the glacial Dwyka Group, the marine Ecca Group and the non-marine Beaufort Group (Smith, 1990; Johnson *et al.*, 2006).

In the Laingsburg depocentre, the 1800 m thick Permian Upper Ecca Group (Fig. 1A) characterizes a marine progradational succession that comprises: (i) distal basin plain deposits of the Vischkuil Formation (Van der Merwe *et al.*, 2009); (ii) basin floor to base-of-slope deposits of the Laingsburg Formation (Units A, A/B and B) (Grecula *et al.*, 2003; Sixsmith *et al.*, 2004; Brooks *et al.*, 2018); (iii) slope channel-levée complexes and entrenched valley deposits of the Fort Brown Formation (Units B/C, C, D, D/E, E, F and G) (Di Celma *et al.*, 2011; Flint *et al.*, 2011; Hodgson

et al., 2011; Brooks *et al.*, 2018); and (iv) shelf-edge deltas of the Waterford Formation (Jones *et al.*, 2015; Poyatos-Moré *et al.*, 2016) (Fig. 1A).

The Laingsburg and Fort Brown formations

The sedimentology and stratigraphic architecture of the Laingsburg and Fort Brown formations are well-constrained through extensive mapping over 2500 km² and numerous outcrop and core studies (e.g. Grecula *et al.*, 2003; Sixsmith *et al.*, 2004; Van der Merwe *et al.*, 2009, 2014; Di Celma *et al.*, 2011; Hodgson *et al.*, 2011; Figueiredo *et al.*, 2013; Morris *et al.*, 2016; Brooks *et al.*, 2018; Poyatos-Moré *et al.*, 2019). Both formations crop out along several east–west trending and eastward plunging, post-depositional anticlines and synclines, around the town of Laingsburg (Fig. 1B). Regional palaeoflow was towards the north-east and the main entry point to the basin was to the south-west (Flint *et al.*, 2011; Van der Merwe *et al.*, 2014). This study focuses on several mid to lower slope depositional units across both formations (Fig. 1A).

The Laingsburg Formation comprises Units A, A/B and B (Fig. 1C). This study examines Unit A/B, which comprises thin-bedded discontinuous sandstones interpreted as a disconnected lobe (Brooks *et al.*, 2018). Unit A/B was supplied sediment by short-lived conduits, such as slope gullies or locally developed incipient channels, which received sediment from slope failures, rather than point-sourced flows through more mature channel-levée systems (Brooks *et al.*, 2018). Furthermore, the restricted planform distribution of Unit A/B in a similar location to younger units with shared sedimentological affinities (for example, B/C and D/E) suggest the presence of subtle seabed topography (Brooks *et al.*, 2018).

The Fort Brown Formation overlies the Laingsburg Formation and comprises Units B/C, C, D, D/E, E, F and G. This study focuses on Units C, D and E, which are interpreted as slope channel-levée systems and intraslope lobe complexes in the proximal outcrops (Flint *et al.*, 2011; Fig. 1C). Unit C contains three channel-levée complexes, subunits C1, C2 and C3, separated by regional mudstones (Di Celma *et al.*, 2011; Flint *et al.*, 2011; Morris *et al.*, 2016), which evolved in a stepwise manner from a weakly incised, levée-confined channel-belt that distributed sediment downdip to a lobe complex (subunit C1) (Di Celma *et al.*, 2011), through a channel-levée complex that avulsed multiple times to feed several submarine lobe complexes (subunit C2) (Morris *et al.*, 2016),

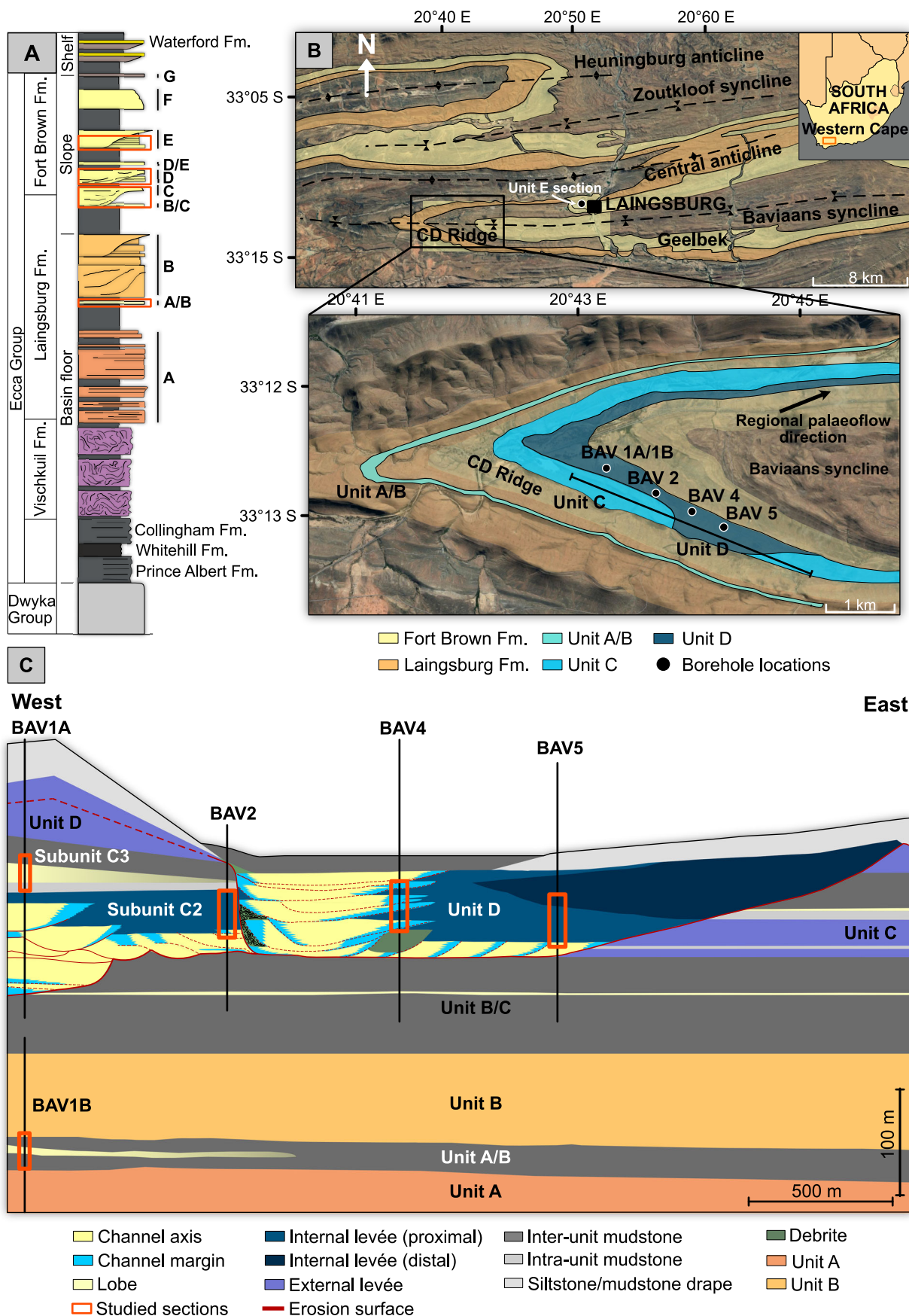


Fig. 1. (A) Stratigraphic column of the Karoo stratigraphy which shows the principal sandstone units of the Laingsburg and Fort Brown formations. Studied units are indicated by the orange boxes. Modified after Boulesteix *et al.* (2022). (B) Satellite images of the Laingsburg depocentre and CD Ridge (zoomed in), which highlight the outcrop extent of the Laingsburg and Fort Brown formations. Studied outcrop areas for each unit are indicated and the locations of the studied boreholes are also labelled. (C) Correlation panel of the CD Ridge outlining the main subunit architectures, depositional environments and borehole locations. The studied sections from each borehole are highlighted in orange boxes. Modified after Morris (2014).

to a regionally backstepping package of thin-bedded deposits (subunit C3), interpreted as a frontal lobe (Morris *et al.*, 2014b).

Unit D is interpreted as an entrenched slope valley that truncates Unit C (Flint *et al.*, 2011). The slope valley is infilled by complicated stratigraphy with many erosion surfaces that characterize an initial phase of westward lateral migration of channels and channel complexes, subsequently followed by a strongly aggradational phase that consists of vertically stacked, sub-symmetrical, amalgamated sand-rich channel-fills (Hodgson *et al.*, 2011, 2016; Fig. 1C). The vertically stacked channel-fills are flanked to the east by thick successions (90–100 m) of laterally extensive thin-bedded SGF deposits, interpreted as an internal levée, deposited within the valley (Kane & Hodgson, 2011; Morris *et al.*, 2016). Outside of the valley, above the main incision surface, Unit D is bounded by external levées (40–70 m thick), which consist of silt-rich SGF deposits that thin and fine away from the valley fill (Kane & Hodgson, 2011; Morris *et al.*, 2014a). In down-dip areas, Unit D becomes fully confined by external levées (Brunt *et al.*, 2013a), before transitioning to unconfined lobe complexes over a down-dip distance of *ca* 80 km (Van der Merwe *et al.*, 2014). A thick mudstone unit overlies Unit D, which is itself overlain by Unit E, which comprises entrenched channel-levée complexes, which incise sand-rich intraslope lobes that formed above a stepped-slope profile (Van der Merwe *et al.*, 2014; Spsychala *et al.*, 2015; Brooks *et al.*, 2018).

NOMENCLATURE

Laminae, laminasets and bedform sequences

Herein, the following terms are used to describe component layers of mixed grain-size bedforms: *laminae*, *laminaset*, *bedform sequence* and *bed* (e.g. Campbell, 1967; Fig. 2). At the smallest-scale, laminae refer to thin layers (1–5 mm thick), that are grain-supported and have

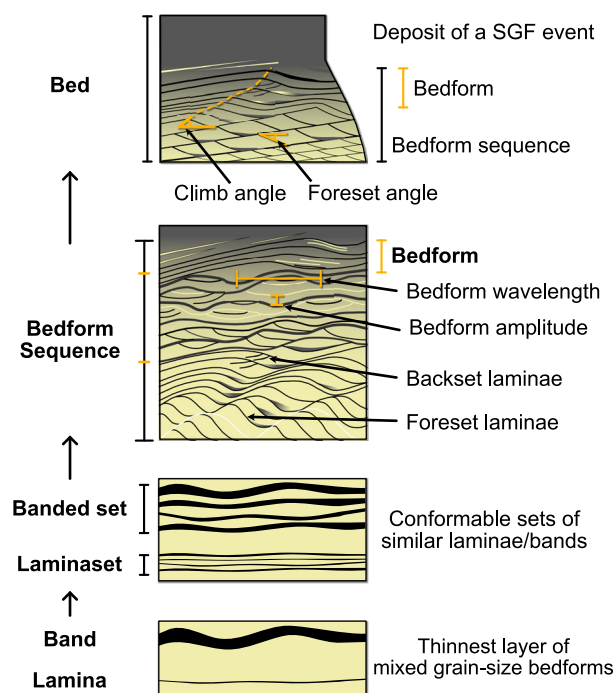


Fig. 2. Diagram highlighting the component layers and terminology used to describe mixed grain-size bedforms in this study. SGF, sediment gravity flow.

relatively sharp upper and lower boundaries, which represent a change in grain size and/or sorting (Campbell, 1967; Best & Bridge, 1992). Notably thicker laminae (5–10 mm thick) are termed *bands* (e.g. Stevenson *et al.*, 2020). Discrete divisions of conformable laminae or bands with similar characteristics are termed *laminasets* or *banded sets*. One or more laminasets with similar properties within a single prograding form are here termed *bedforms*. At a location, a bedform can be represented by a single laminaset, thus bedform and laminaset can be synonymous. Bedforms with different textural and morphological properties stack to form *bedform sequences*, which make up parts of *beds* (the deposit of a single sediment gravity flow event). Beds do not necessarily have to contain

bedform sequences (i.e. more than one bedform), because a single bedform can represent an entire event bed. Successions of similar bed types comprise sedimentary *facies*. Associations of different facies (*facies associations*), with upper and lower bounding surfaces, stack to form a geometrically distinct body, and are used in combination with stratigraphic context and mapping to interpret depositional environments.

Mud and cohesivity

Mud is employed as a general term for a mixture of clay-sized and silt-sized particles (McCave *et al.*, 1995; Winterwerp & van Kesteren, 2004), and to describe laminae that are rich in grain sizes <63 µm diameter. Cohesive forces become more significant between clay particles <30 µm diameter (McAnally *et al.*, 2007) and non-cohesive particles, such as quartz grains <10 µm diameter, are affected by van der Waals forces that produce similar, albeit less robust, attractions between grains (McCave *et al.*, 1995).

DATASET AND METHOD

This study utilized over 100 m of core from five research boreholes (BAV 1A, BAV 1B, BAV 2, BAV 4 and BAV 5), drilled across the CD Ridge to the south-west of the Laingsburg depocentre (Fig. 1B). Key sections were identified through well-constrained depositional environments that contained distinct mixed grain-size bedforms (Fig. 1C): BAV 1A intersects Unit C3, interpreted as a frontal lobe (Morris *et al.*, 2014b); BAV 1B intersects Unit A/B, interpreted as a disconnected lobe (Brooks *et al.*, 2018); BAV 2 intersects a 27 m thick internal levée section of Unit C2 (Morris *et al.*, 2016); BAV 4 intersects a 26 m thick channel margin/proximal internal levée section of Unit D (Flint *et al.*, 2011); and BAV 5 intersects a 76 m thick distal internal-levée section of Unit D (Morris, 2014). Outcrop sections of Units A/B, C2, C3, D and E (interpreted as an intraslope lobe), were also examined at broadly similar intervals (Fig. 1B), to constrain palaeoflow direction, planform geometry of bedforms and dimensions of bedforms too large to be measured from core sections.

Candidate core and outcrop sections were logged at 1 : 1 and 1 : 20 scale, respectively, to record the stratigraphic distribution of bedforms and bedform sequences. Detailed observations of their laminasets included: the geometry of the

constituent laminae, such as their shape, size and climb angle (Fig. 2); and their texture, such as the distribution of mud and sand. Palaeoflow direction from core was based on the basal contact geometry of foreset laminae and calibrated with outcrop observations. A *Dino-Lite Edge* digital microscope (AnMo Electronics Corporation, Hsinchu City, Taiwan) was used to acquire high-resolution core micrographs to support grain-size and sorting descriptions across individual laminae and laminasets. Visual identification of grains from scaled core micrographs showed that the darker mud-rich laminae were rich in grain sizes <30 µm. The elevated mud content in darker laminae is also supported by previous petrographic studies on the same cored sections as studied here, which demonstrated that darker laminae comprise clay and silt <10 µm (Boulesteix *et al.*, 2022). Kane *et al.* (2017) also showed that SGF deposits from broadly equivalent intervals in the Tanqua depocentre, Karoo Basin, contain 10 to 35% detrital clay. Therefore, deposit colour provides a useful indication of grain size, and mud laminae, identified by visual identification, contain elevated clay, or grains that were small enough to form cohesive forces in the flow from which they were deposited. Photogrammetric models of some core and outcrop sections were generated using a LiDAR-enabled, *Apple iPhone 12 Pro* (Apple, Cupertino, CA, USA), which captured the three-dimensional geometry and planforms of the bedforms. Sedimentary processes for candidate bedform types were then interpreted based on key distinctions in their laminaset shape, size and texture.

Sedimentary facies scheme

The stratigraphy of the Laingsburg and Fort Brown formations is described using a sedimentary facies scheme modified from previous studies of the Laingsburg depocentre (Di Celma *et al.*, 2011; Hodgson *et al.*, 2011; Brunt *et al.*, 2013a,b; Morris *et al.*, 2014a,b; Brooks *et al.*, 2018; Boulesteix *et al.*, 2022). Six sedimentary facies are defined that characterize the main depositional environments. For each facies, their process interpretation, representative core photograph and depositional environments are shown in Table 1. This study focuses on Facies 2 (mixed grain-size structured sandstones), which contain the bedforms discussed herein. The other sedimentary facies provide further context for the depositional setting (Table 1).

Table 1. Facies descriptions (F1–F6), process interpretations and representative core photographs.




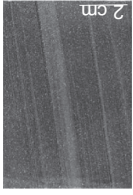

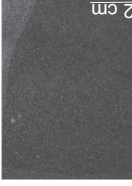
Code	Facies	Grain size	Bed characteristics	Structures	Process interpretation	Depositional environment	Core photograph
F1	Structureless sandstone	Fine to very fine-grained sand, normal grading	0.15 to 1.5 m thick. Sharp, erosional bases sometimes loaded. Commonly amalgamated	Mostly structureless. Rare occurrences of planar lamination. Bed bases sometimes have mud-clast layers and flame structures. Rare, contorted bedding present	Rapid suspension settling from fully turbulent high-density sediment gravity flows (e.g. Bouma, 1962; Lowe, 1982). Flame structures at the bases of structureless beds are representative of syn-depositional or post-depositional dewatering (Stow & Johansson, 2000). Deformation is attributed to slumping and remobilisation of soft sediments. Mud clasts are interpreted as lag deposits and suggest prolonged erosion (Kneller, 1995)	Channel axis, channel margin	
F2	Mixed grain-size structured sandstone	Fine-grained sand to fine silt and mud	0.05 to 0.5 m thick. Distinctive rippled bed types which can be laterally continuous for tens to hundreds of metres. Sharp, sometimes erosional bases	Beds comprise a range of mixed grain-size bedforms consisting of low to high angle, mud-rich cross-lamination or banding which can have asymmetrical or hummock-like and swale-like geometries	Mixed grain-size bedforms indicate deposition from rapidly decelerated, cohesive transitional flows (Baas <i>et al.</i> , 2016). Variations in laminaset geometry suggest interactions with seabed topography that generate combined (but still transitional) flows (Tinterri, 2011). See text for full interpretations	Proximal basin settings: channel margin, internal levée, external levée, frontal lobe, disconnected lobe	
F3	Thin-bedded sandstone	Very fine-grained sand. Normal grading	0.05 to 0.15 m thick. Thinning upward trend. Sometimes laterally discontinuous. Sharp, sometimes erosional bases	Planar lamination, sand-rich, low to high angle climbing ripple cross-lamination. Some wavy bedforms	Suspension settling from fully turbulent, low density sediment gravity flows with sustained bedload transport (Allen, 1971). Sand-rich, low-angle climbing ripples indicate higher rates of migration and lower rates of suspension settling than facies F2 (Jobe <i>et al.</i> , 2012)	Channel margin	

Table 1. (continued)

Code	Facies	Grain size	Bed characteristics	Structures	Process interpretation	Depositional environment	Core photograph
F4	Thin-bedded siltstone	Very coarse to fine-grained silt, normal grading	0.01 to 0.1 m thick. Thinning upward trend. Sharp bases	Mostly structureless, some wavy (sinusoidal) and planar 'starved lamination'	Deposition from dilute, low-density turbidity currents (Bouma, 1962), or decelerated, cohesive transitional flows (Baas <i>et al.</i> , 2016). High sediment fallout rates are inferred from the presence of highly aggradational bedforms (e.g. Jopling & Walker, 1968; Ashley <i>et al.</i> , 1982; Baas <i>et al.</i> , 2021a)	Distal internal levée, external levée	
F5	Faintly bedded mudstone	Very fine-grained silt to clay, subtle grading	0.0003 to 0.01 m thick. Poorly defined bed boundaries.	Mostly structureless	Deposition from the distal extents of dilute sediment gravity flows. This facies is analogous to 'Facies 2: faintly bedded mudstones' of Boulesteix <i>et al.</i> (2022)	Slope mudstones (internal levée, external levée, frontal lobe)	
F6	Massive mudstone	Very fine-grained silt to clay.	Massive. Few centimetres to several metres thick. Sharp bases	Mostly structureless	Hemipelagic sedimentation which indicates periods of local or regional shutdown of sediment supply. May also represent the distal expression of transitional flows as they transform from turbulent to laminar (Baker & Baas, 2020), following observations from Boulesteix <i>et al.</i> (2022)	Lower slope to basin floor mudstones (external levée, disconnected lobe)	

MIXED GRAIN-SIZE BEDFORMS

The following section presents observations and process interpretations of mixed grain-size bedforms from the studied core and outcrop sections. They are grouped into two bedform types (Type A and Type B), based on differences in their shape, size, texture and internal stratification. A brief description of observed sand-rich current ripples, associated with non-cohesive sediment (Table 1, F3), is first provided for comparison.

Sand-rich current ripples

Sand-rich current ripples are characterized by their asymmetrical shape which consists of a gentle stoss slope and a shorter and steeper lee slope. Their foreset laminae consist of very-fine to fine-grained sandstone. Locally, sand-rich current ripples contain concave-up or planar foresets with high termination angles (*ca* 28°) against the bases of individual laminasets (Table 1, F3). They form distinct trains of low-angle climbing sandstone foreset laminae that thin upward and transition to high-angle climbing variants where the stoss-side of the ripple is preserved. High-angle climbing variants have sharp ripple tops. Sand-rich current ripples are observed in Facies 3 (Table 1) and are interpreted to form from tractional reworking under low-density, fully turbulent sediment gravity flows, and comprise the T_c division of typical Bouma-type beds (Bouma, 1962; Allen, 1971).

Type A Bedforms

Mud-rich current ripples

Asymmetrical, climbing laminasets that contain distinct, high-angle, concave or planar foreset laminae of mixed or alternating sandstone–mudstone, are referred to as mud-rich current ripples (Fig. 3). Typically, the mud-rich foreset laminae are thin (<1.5 mm thick) but tend to thicken as they pass into ripple troughs (Fig. 3A). Trough-fills are more mud-rich than the foresets and generally coarsen upward. In some cases, laminasets contain mud-rich foresets that thin and fine into more sand-rich trough-fills (Fig. 3J). Locally, subtle erosion surfaces are observed at the base of climbing laminasets and in trough-fills. Core micrographs taken across trough-fills reveal a mix of grain sizes from coarse silt to clay, although grains less than 30 µm diameter are most common (Fig. 3).

Mud-rich current ripples are mostly high-angle climbing with stoss-side preservation, but also

form trains of low angle-climbing concave laminasets (Fig. 4A). As climb angle increases, the foreset laminae become muddier and thicker, and their wavelength and amplitude increase (Figs 3G and 4A). Rarely, millimetre-scale backset laminae are observed on lee side foresets (Fig. 3E and F). Locally, mud-rich foresets are sometimes loaded by thicker sand-rich laminae, with a ‘kinked’ appearance (Fig. 3H and I).

In core, the wavelengths (the horizontal distance between adjacent bedform troughs, Fig. 2) of mud-rich current ripples were difficult to capture due to the limited width of the core. However, some minimum values of bedform amplitude (the vertical distance between bedform trough and crest, Fig. 2) could be measured and ranged between 7 to 25 mm. At more complete outcrop sections, average amplitudes across different laminasets ranged between 10 to 30 mm, while wavelengths ranged between 140 to 200 mm (Fig. 4). When compared to sand-rich current ripples, the mud-rich current ripples observed in this study are larger in both their wavelengths and amplitudes but maintain similar aspect ratios (Fig. 4). Some, but not all mud-rich current ripples are in the same size range as so-called ‘large current ripples’, produced experimentally and documented from the distal fringes of submarine fans (Baas *et al.*, 2016; Baker & Baas, 2020).

Low-amplitude bed-waves

Low-amplitude bed-waves (LABWs) are comprised of asymmetrical, low-angle (Fig. 5A and B) and occasionally high-angle climbing laminasets with stoss-side preservation (Fig. 5D) that contain gently dipping and alternating sandstone–mudstone foreset laminae (Figs 4 and 5), following Baas *et al.* (2016). The foresets are thin (<1 mm thick), low angle (*ca* 10°), and commonly pass into mud-rich trough-fills that weakly coarsen and thin upward (Fig. 5A). Some examples contain mud-rich foresets that pass into sand-rich trough-fills, as with the mud-rich current ripples.

The LABWs were found in mud-rich packages, such as at the tops of mixed grain-size beds or isolated in thick mudstones (Figs 4A and 5). In core, the full profile of LABWs were rarely captured due to their long wavelengths. However, some key diagnostic features that aided their identification included the low-angle mudstone foresets (Fig. 5D and E) and their association with very thin (1–2 mm), laterally discontinuous sand-rich laminae that pinch out over 50 mm. These laminae form a streaky texture, herein termed ‘starved lamination’ (Fig. 5A).

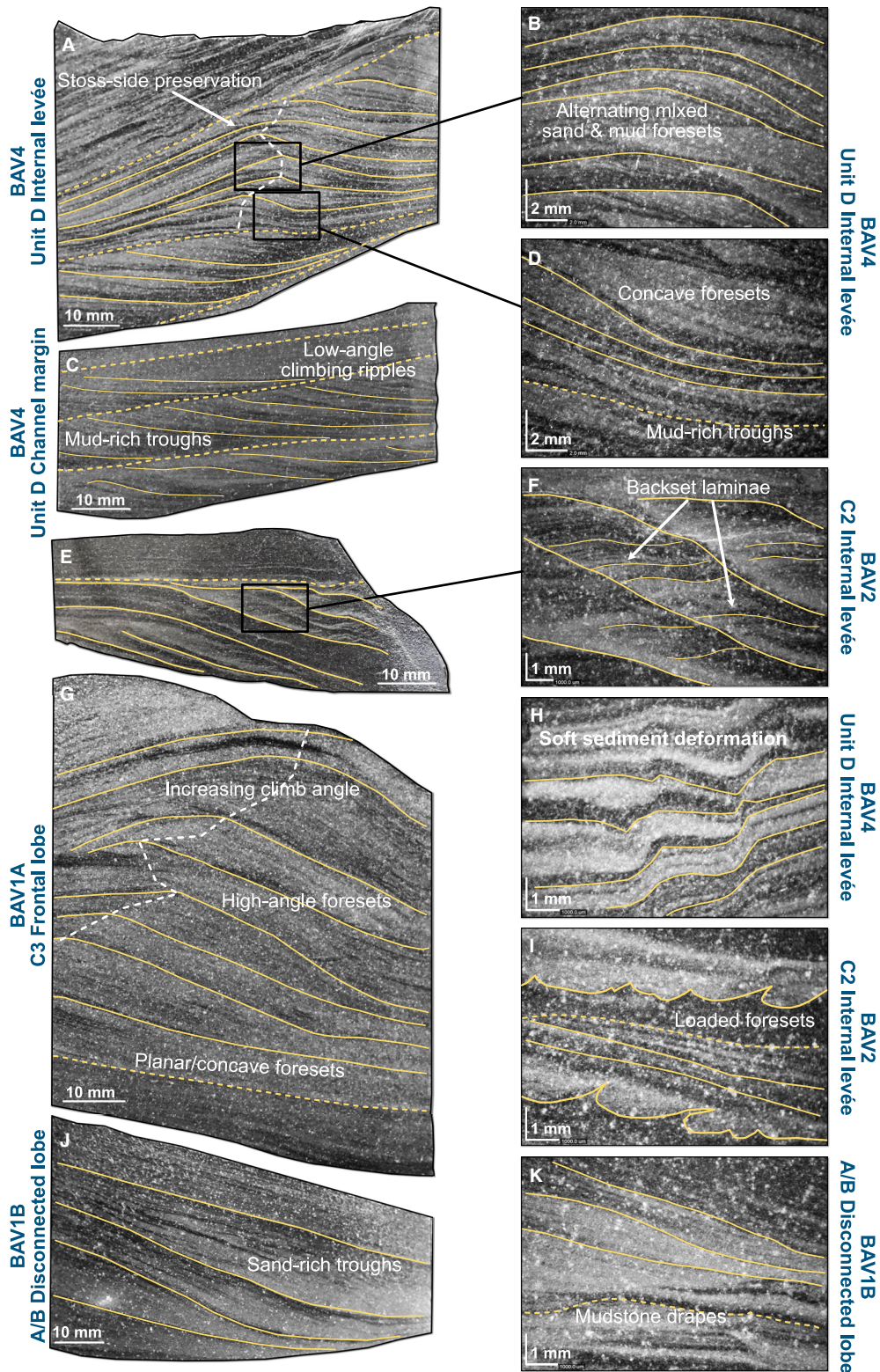


Fig. 3. Representative high-contrast, annotated core images which show some of the characteristic features of Type A mud-rich current ripples. Solid yellow lines indicate examples of foreset laminae. Dashed yellow lines indicate laminaset boundaries. White dashed lines trace ripple brinkpoints, indicating variations in climb angle across laminasets. The left column shows photographs taken with a macro lens, while the right column shows micrographs taken with a digital microscope.

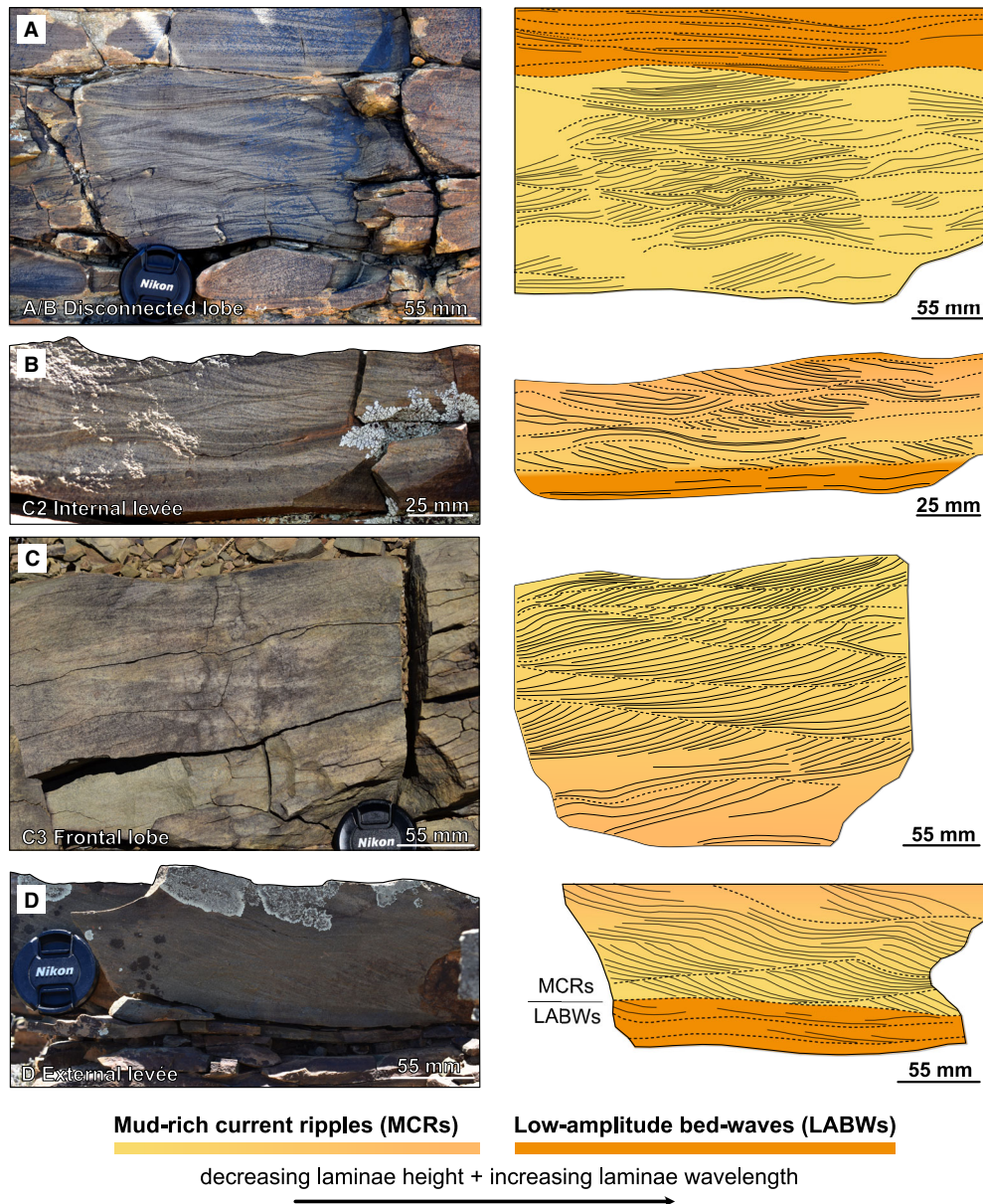


Fig. 4. Representative outcrop photographs and drawn interpretations which highlight internal laminasets and transitions of Type A bedform sequences within: (A) disconnected lobe; (B) internal levée; (C) frontal lobe; and (D) external levée depositional environments. Lens cap is 55 mm in diameter. Solid lines represent foreset laminae and dashed lines represent laminaset boundaries.

The LABWs have higher aspect ratios when compared with the other bedform types. At outcrop, where the entire bedform profile could be observed, average wavelengths across different laminasets ranged between 120 mm and 400 mm, with amplitudes between 7 mm and 12 mm (Fig. 4A), and formed sharp, linear to sub-linear crest lines in planform (Fig. 6), which are similar to other observations of LABWs in distal settings

(Baker & Baas, 2020). When compared to mud-rich current ripples, LABWs have higher aspect ratios with similar wavelengths, albeit smaller amplitudes.

Sinusoidal lamination

Sinusoidal laminasets are long, thin, wavy bedforms, and are like LABWs in that they consist of very thin, alternating sandstone–mudstone

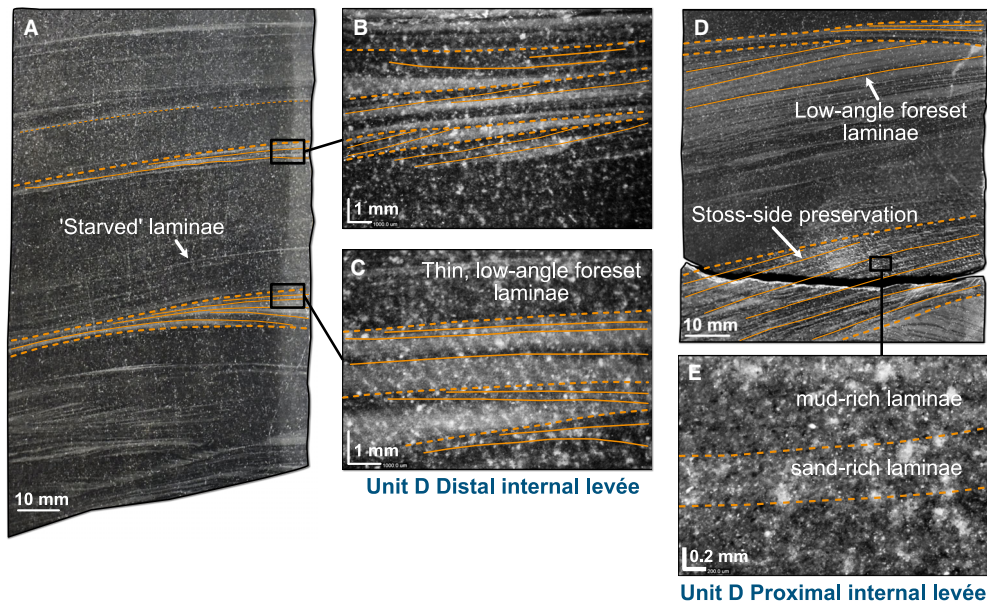


Fig. 5. Representative high-contrast, annotated core images which highlight some of the structural and textural properties of low-amplitude bed-waves (LABWs). Solid lines indicate examples of low-angle foreset laminae. Dashed lines indicate laminaset boundaries. Images (A) and (D) are photographs taken with a macro lens. Images (B), (C) and (E) are micrographs taken with a digital microscope.

laminae (Fig. 7). In contrast, sinusoidal laminasets are highly aggradational, where climb angles typically exceed 45° (Fig. 7A). Unlike LABWs, the stoss-side and lee-side laminae have similar thicknesses and angles, which reflect their characteristic sinusoidal shape (Fig. 7B, D and E). Sinusoidal laminasets were observed at finer-grained tops of mixed grain-size beds, and within thicker mudstone packages (Fig. 6A). As climb angle increases upward within laminasets, the wavelength of sinusoidal laminae remains constant in some beds, while in rare examples, the wavelengths appear to lengthen as the bed grades normally upward (Fig. 7C).

Process interpretation of the Type A bedforms

Type A bedforms comprise significant, and variable, proportions of mud in their laminasets. Therefore, their process interpretation requires consideration of the balance between flow-velocity controlled turbulent forces and clay-derived cohesive forces (Baas *et al.*, 2009; Sumner *et al.*, 2009). Laminasets comprised of alternating mud-rich and sand-rich laminae are therefore interpreted as the depositional record of transitional flows that carried substantial cohesive mud. On undergoing rapid deceleration, flow turbulence decreases due to increased cohesive forces. As a flow decelerates,

cohesive clay particles in suspension begin to form flocs and gels due to electrostatic forces between individual particles, which act to increase flow yield strength and viscosity, and thus dampen flow turbulence (e.g. Wang & Plate, 1996; Lowe & Guy, 2000; Baas & Best, 2002; Haughton *et al.*, 2003; Talling *et al.*, 2004). The suppression of turbulence sets up a transitional flow, which passes through several different transitional flow phases as cohesive forces increase. These flow phases, from turbulent to laminar, as referred to by Baas *et al.* (2009), comprise turbulence-enhanced transitional flows (TETF), lower transitional plug flows (LTFP), upper transitional plug flows (UTPF) and quasi-laminar plug flows (QLPF). The Type A bedforms observed here closely resemble the cohesive, mixed sand-silt-clay bedforms identified from earlier experimental work (Baas *et al.*, 2016) and outcrop observations (Baker & Baas, 2020).

Mud-rich current ripples bear close resemblance to the so-called 'large ripples' of Baas *et al.* (2016) due to their alternating sand-mud foreset laminae, mud-rich trough-fills, and greater amplitudes (Fig. 3) and wavelengths than sand-rich ripples formed from non-cohesive, turbulent flows. Therefore, mud-rich ripples are interpreted to have formed under TETF and LTFP conditions (Baas

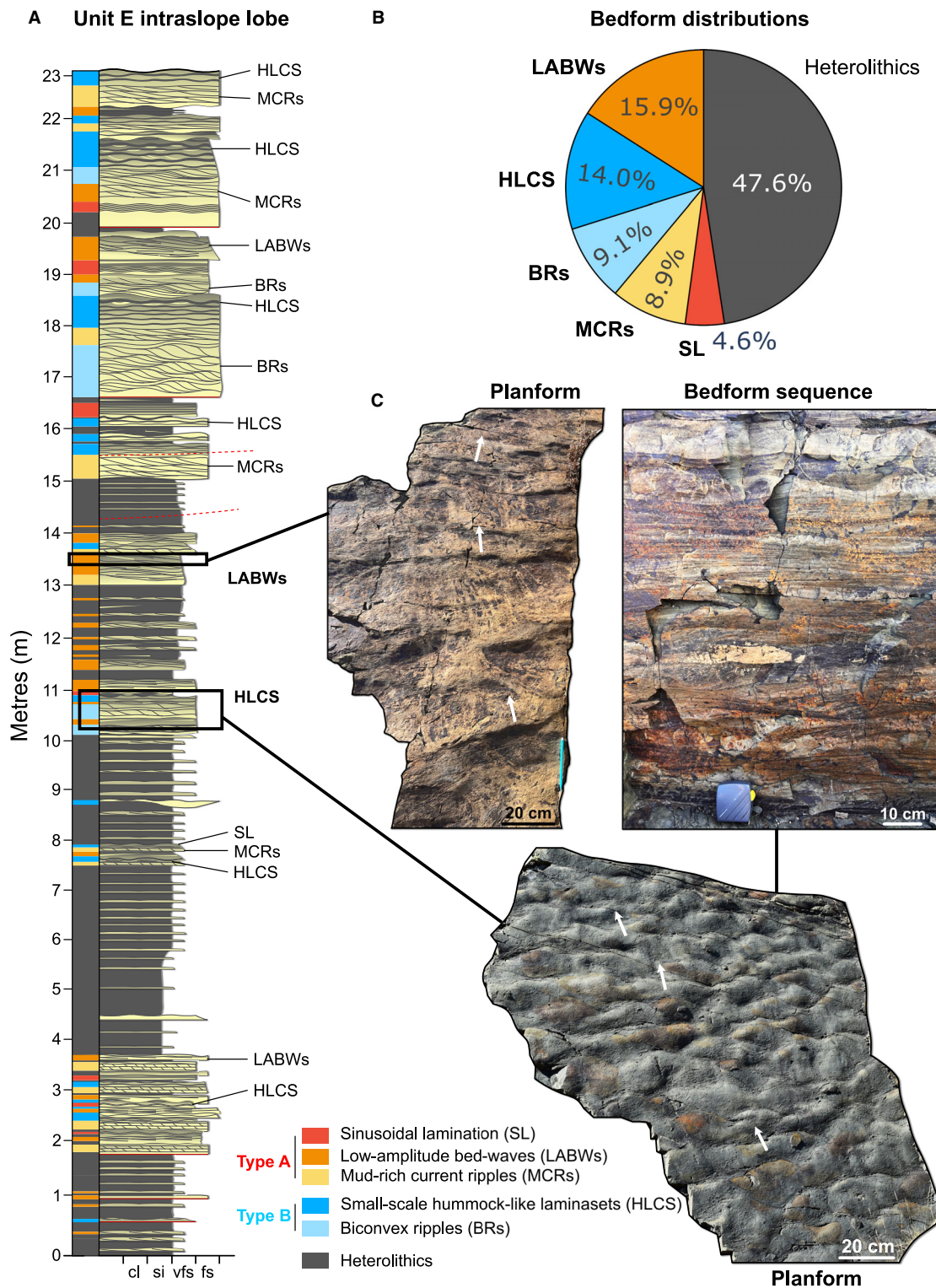


Fig. 6. (A) Representative sedimentary log of the Unit E intraslope lobe outcrop section showing the different bedform types and vertical transitions. Location: UTM 34H 486347 632705 (Fig. 1B). (B) Pie chart showing the thickness proportions of the different bedforms from the logged section. Percentage values are rounded to one decimal place. (C) Representative images from key beds showing the planform surfaces and bedform sequences. Arrows show palaeocurrent directions (NNW–NNE).

et al., 2011). TETF conditions are strongly turbulent throughout the flow depth, with local turbulence enhancement in ripple troughs, which helps to increase ripple size (Baas & Best, 2008). This occurs through an initial increase in flow cohesion from the decelerating flow, which generates an internal shear layer and drives erosion on the lee side of the bedform, promoting increased bedform amplitude. This local turbulence increase is supported by the presence of backset laminae on the lee foresets (Fig. 3E), which reflect strong vorticity and upstream flow velocities in the ripple troughs (Baas *et al.*, 2011, 2021a).

An increase in climb angle upward through mud-rich current ripple laminasets (Fig. 3G) indicates increasing sediment fallout rates relative to migration rate during deposition (Allen, 1973; Jobe *et al.*, 2012). An upward increase in the proportion of mud-rich laminae in a single laminaset suggests increasingly intermittent bedload transport of coarser grains by avalanching down the lee slope, to a more continuous supply from suspension of finer grains as the flow decelerates. Where individual foreset laminae are muddier and the troughs sandier (i.e. a positive mean grain-size gradient across the ripple), the coarser grains are interpreted to avalanche further down the lee slope than the finer particles (Fig. 3J). In this case, the effects of grain avalanching outweigh the effects of suspension settling, which may indicate temporary waxing flow conditions (Allen, 1968).

The observation of LABWs in mud-rich sections near bed tops or isolated in mudstone packages (Figs 5 and 6A), supports an interpretation of higher mud content in the decelerating flow, and suggests higher flow viscosity and significant sediment fallout from suspension. This results in longer and thinner laminasets than those formed under turbulent and turbulence-enhanced transitional flows (Baas *et al.*, 2011, 2016). Therefore, LABWs are here interpreted to form under LTPF to UTPF conditions. Under these conditions, cohesive forces begin to influence flow structure, and electrostatic bonding between clay particles initiates a plug-flow region with, or without, a very low vertical gradient in streamwise velocity, and a lack of turbulence, which expands downward as cohesion increases (Baas *et al.*, 2009).

Sinusoidal laminasets are observed at bed tops. Their steep climb angles indicate strong increases in suspension fallout rate (Allen, 1973) and a significant reduction in migration rate after high rates of flow deceleration (Jopling & Walker, 1968). Therefore, they are inferred to form under UTPF and QLTPF conditions (Baas *et al.*, 2021a), which

are characterized by further downward expansion of the plug-flow region and loss of turbulence in the underlying shear layer, as clay-derived cohesive forces increase. Therefore, the shear layer ceases to provide sufficient turbulence to break bonds between clay particles and produces a slow-moving, depositional, quasi-laminar plug flow (Baas *et al.*, 2009).

Type B Bedforms

Rounded, biconvex ripples

Rounded, biconvex ripples are symmetrical to slightly asymmetrical with rounded profiles and sigmoidal-shaped foreset laminae of alternating sandstone–mudstone (Figs 8 and 9). The foresets are variable in thickness and have low-angle, tangential bases that drape mostly erosional lower laminaset bounding surfaces (Fig. 9E). Mud is concentrated on the sigmoidal-shaped foresets, rather than in the trough-fills, and mud-rich foresets are usually thicker and more continuous than sand-rich foresets (Fig. 8B). The trough-fills are thinner than Type A mud-rich current ripples and contain a mixture of sand and silt–clay grains that coarsen upward. Locally, the rollovers of laminasets are draped by 2 to 3 cm thick laterally discontinuous mudstone (Fig. 8D).

Biconvex ripples are either low-angle climbing, and form trains of sigmoidal cross-laminasets, or high-angle climbing with stoss-side preservation. With increasing climb angle, foreset laminae become increasingly mud-rich and thicker (Fig. 8E). The average climb angle for this bedform type was 38°, laminae wavelengths typically ranged between 40 to 200 mm, and bedform amplitudes ranged between 8 to 30 mm (Fig. 9).

Hummock-like and swale-like laminae and banded sets

Laminasets that resemble hummock-like cross-stratification (HLCS) are erosively-based, low to high-angle laminae and banding that are concave-up and convex-up, which represent small-scale swale-like and hummock-like features, respectively (Fig. 10, Videos 1 and 2). The laminae and bands described here generally do not present cross-cutting relationships between sets of swales and hummocks, and upward transitions within a laminaset are gradual and continuous (Video 2), in contrast to conventional hummocky cross-stratification (Harms, 1969). The hummock-like features at the tops of laminasets are also smaller and tighter than conventional hummocky cross-stratified structures (e.g. Harms *et al.*, 1975). At

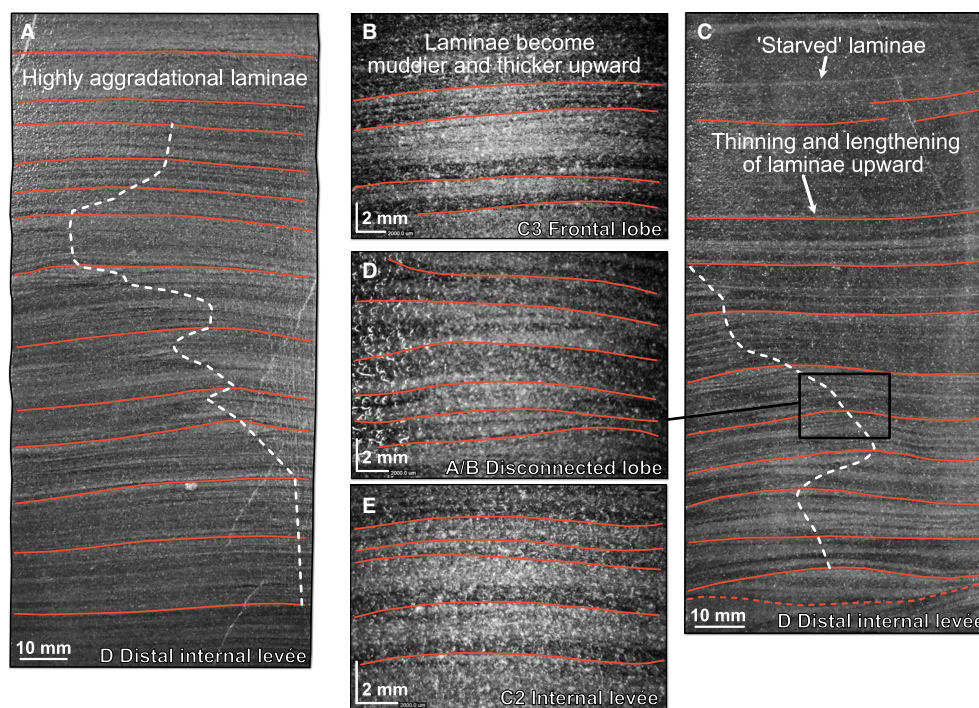


Fig. 7. Representative high-contrast, annotated core images which show some of the textural and structural properties of sinusoidal laminasets. Solid lines indicate some of the laminae outlines. White dashed lines trace laminae brinkpoints. Images (A) and (C) are photographs taken with a macro lens. Images (B), (D) and (E) are micrographs taken with a digital microscope.

laminaset bases, the laminae are typically swale-like and erosional (20–30 mm deep), and hummock-like towards the top (Fig. 10E). Internally, HLCS laminasets contain mixed and alternating sandstone–mudstone laminae, which tend to drape lower bounding surfaces tangentially at low angles ($<20^\circ$), or in some cases are fully continuous (Fig. 10D, Video 1). Mud-rich laminae can drape the rollovers of individual hummocks. Locally, the laminae can exceed 5 mm thick, and thus resemble sandstone–mudstone banding (Fig. 10C, Video 2). The tops of the banded sets are sometimes overlain by LABWs and sinusoidal laminasets (Fig. 10D). The swale-like and hummock-like geometry is most apparent when core sections were viewed in three dimensions (Videos 1 and 2).

The HLCS laminasets have wavelengths that exceed the width of the core. At outcrop sections, bedform amplitudes ranged between 30 mm and 100 mm, with wavelengths that ranged between 130 mm and 250 mm (Fig. 9). The planforms of HLCS laminasets exhibited rounded hummock-like crests and swale-like troughs that are distinct from the sharp crests and linear to sub-linear tops

of mud-rich current ripples and LABWs. Some examples of the HLCS planforms were more elongated than conventional hummocky cross-stratified structures (Fig. 6C), while others exhibited more mounded, three-dimensional forms.

Process interpretation of the Type B bedforms

The Type B bedforms are interpreted to form underneath combined flows (Harms, 1969; Arnott & Southard, 1990; Yokokawa *et al.*, 1995; Tinterri, 2011). Yokokawa *et al.* (1995) showed experimentally that oscillatory flows, combined with a strong unidirectional component (at 180° to the wave direction) produced small-scale biconvex ripples with sigmoidal-shaped foresets. The formation of these foresets was linked to the redistribution of sand by vortices on the lee side of the ripple related to the uneven forward and backward strokes of the oscillatory flow components. The top of the lee side of the ripple would become preferentially ‘nourished’ by sand, and ultimately contribute to the rounded, biconvex profile (e.g. Tinterri, 2011). In ancient deep-marine settings, laminasets that exhibit similar rounded profiles with sigmoidal foresets are commonly associated

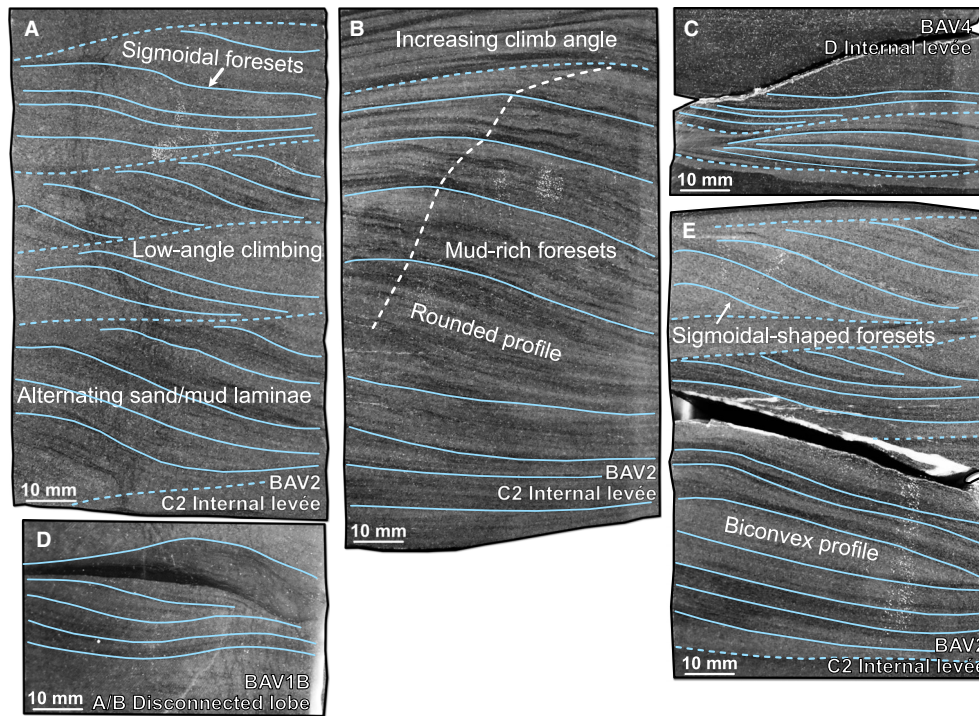


Fig. 8. Representative high-contrast, annotated core images of biconvex ripples. Blue solid lines indicate representative examples of laminae outlines and foreset laminae. Blue dashed lines indicate laminaset boundaries. White dashed lines trace laminae brinkpoints, indicating variations in climb angle across laminasets.

with beds where sediment gravity flows have interacted with topography (Pickering & Hiscott, 1985; Haughton, 1994; Tinterri & Muzzi Magalhaes, 2011; Hofstra *et al.*, 2018; Privat *et al.*, 2021; Tinterri *et al.*, 2022). Therefore, the generation of biconvex ripples points to the interaction of mud-rich transitional flows with topography, which set up a combined flow, initially with a strong unidirectional component.

The flows that formed the biconvex ripples must also have contained cohesive sediment and decelerated rapidly, resulting in the alternating sand-rich and mud-rich laminae. Therefore, it is unlikely that these laminasets are the product of washed-out ripples, which form under high near-bed suspended sediment concentrations at the transition from ripples to upper-stage plane beds (Baas & De Koning, 1995). Furthermore, while small-scale antidunes that form under strongly unidirectional supercritical flows (Alexander *et al.*, 2001; Cartigny *et al.*, 2014; Fedele *et al.*, 2016) can exhibit biconvex profiles and convex foreset laminae, this does not explain the observed laminae-scale segregation of grain sizes. In addition, previously documented examples of antidunes are more frequently concave than convex, tend to dip upstream rather than

downstream (Cartigny *et al.*, 2014), and are typically much larger (decimetre to metre-scale) than the biconvex ripples observed here, which tend to dip in the same direction as regular unidirectional sand-rich current ripples and mud-rich current ripples (Postma & Kleverlaan, 2018; Cornard & Pickering, 2019).

The HLCS laminasets and banded sets are similarly interpreted to form under combined flows with unidirectional–oscillatory components (Dumas *et al.*, 2005), because they largely resemble isotropic and anisotropic hummocky cross-stratification (HCS) (Dumas & Arnott, 2006). The laminasets and banded sets with high-angle internal laminae ($>20^\circ$) that drape lower bounding surfaces (Fig. 10G), are broadly comparable to anisotropic HCS (Dumas & Arnott, 2006), where the combined flow has a much smaller unidirectional component than biconvex ripples. Where internal laminae dip at much lower angles ($<15^\circ$), or do not terminate against lower bounding surfaces (i.e. fully continuous), such structures may resemble isotropic HCS (Fig. 10F), where flow is fully oscillatory with a negligible unidirectional component (Harms *et al.*, 1975; Dumas & Arnott, 2006; Tinterri, 2011). Whilst the HLCS

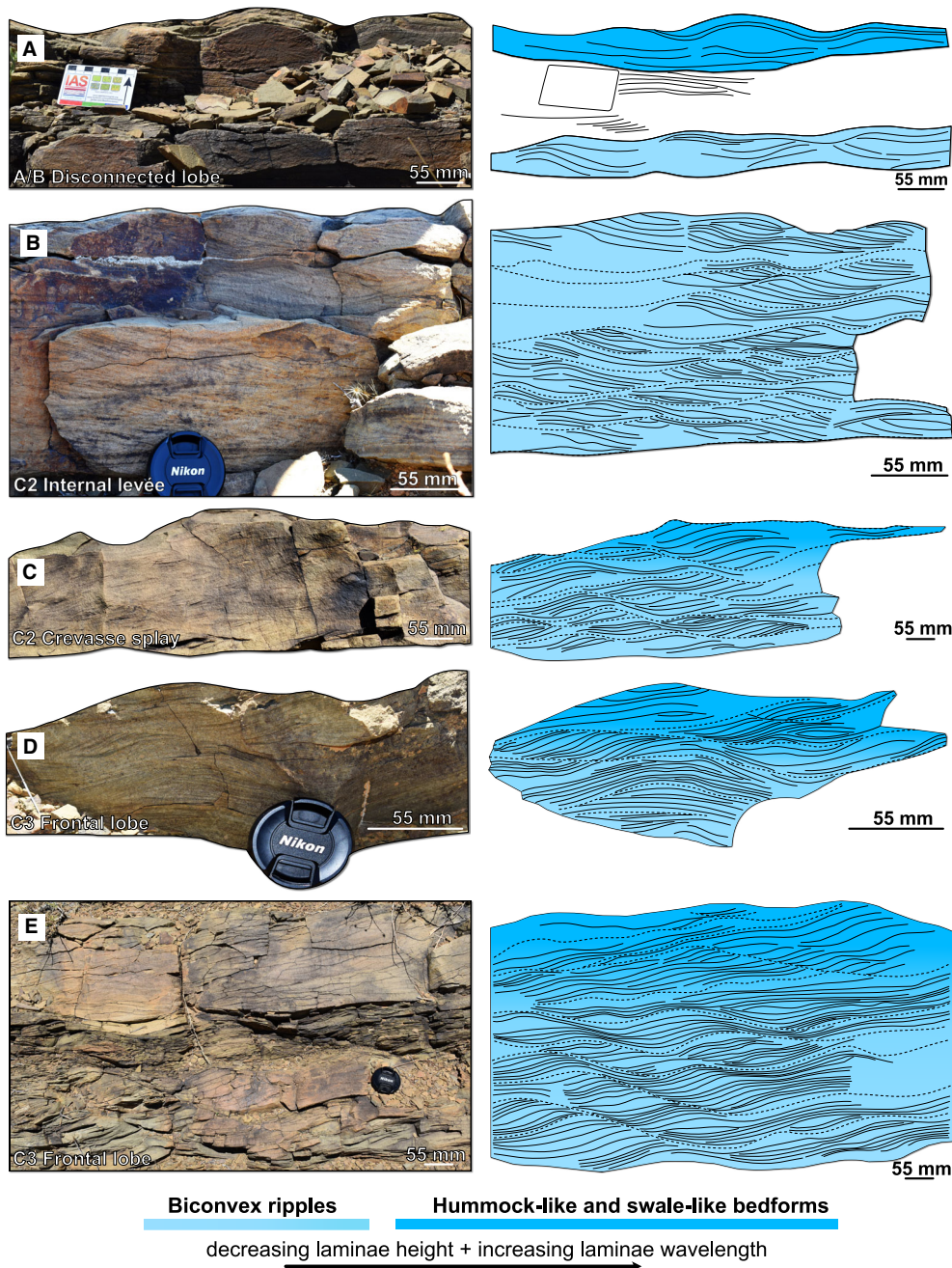


Fig. 9. Representative outcrop photographs and drawn interpretations which show internal laminasets and transitions of Type B bedform sequences within: (A) disconnected lobe; (B) internal levée; (C) crevasse splay; and (D) and (E) frontal lobe depositional environments. Lens cap is 55 mm in diameter. Solid lines represent individual laminae and dashed lines represent laminasets boundaries.

laminasets and banded sets documented here share some similarities with conventional HCS, they do not necessarily present cross-cutting relationships between individual laminae of swales and hummocks, and upward transitions within laminasets are gradual and continuous, unlike

HCS structures that form above storm-wave base (e.g. Harms *et al.*, 1975; Jelby *et al.*, 2020). Examples of similar structures documented in deep-marine environments, such as basin plain and channel-lobe transition zones, are interpreted as the product of flow deflection off topography

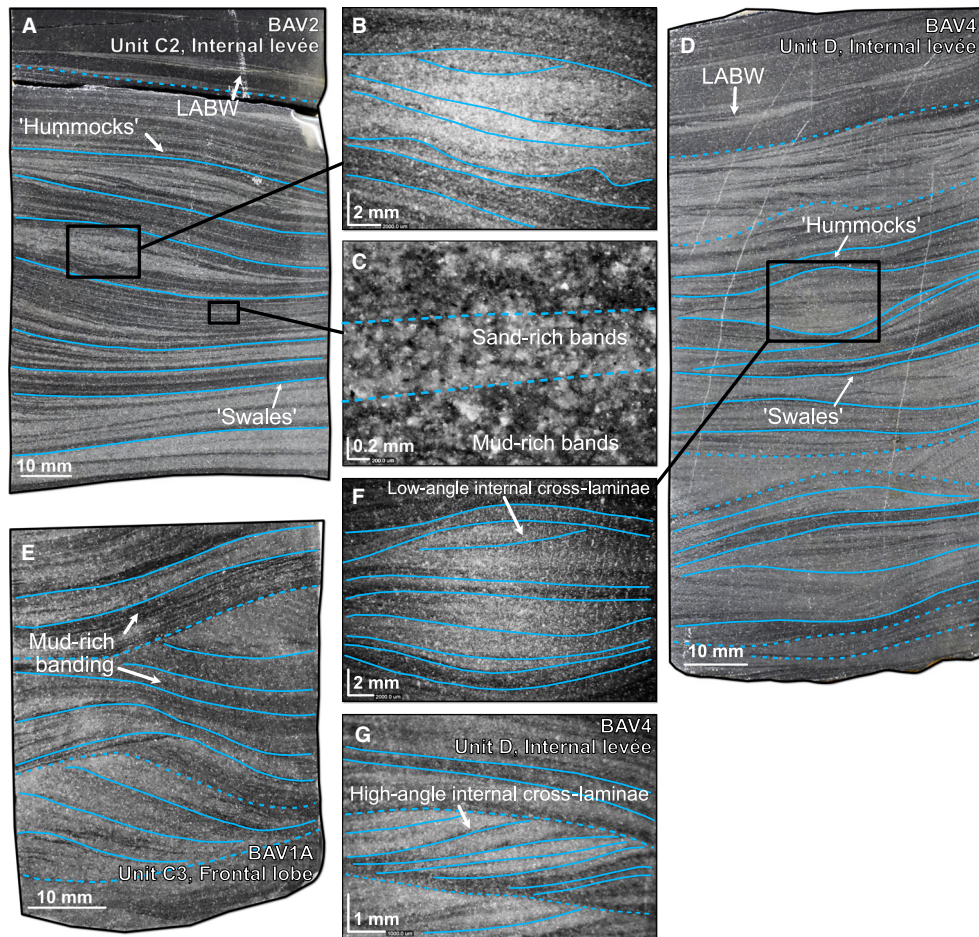


Fig. 10. Representative high-contrast, annotated core images of small-scale hummock-like and swale-like laminae and banded sets (HLCS). Solid lines indicate laminae or banded hummocks and swales. Dashed lines indicate lamina-set boundaries. Images (A), (D) and (E) are photographs of HLCS laminasets taken with a macro lens. Images (B), (C), (F) and (G) are micrographs of HLCS laminasets taken with a digital microscope. LABW, low-amplitude bed-wave.

(Tinterri & Muzzi Magalhaes, 2011; Bell *et al.*, 2018; Hofstra *et al.*, 2018; Tinterri *et al.*, 2022). As with biconvex ripples, an alternative is that small-scale HLCS resemble antidunes (Prave & Duke, 1990; Cartigny *et al.*, 2014). Typically, antidunes are characterized by their rounded convex profiles, concave-up erosive surfaces, extensive cross-cutting laminasets (if unstable antidunes), gently dipping upstream laminae (if upstream migrating), low angle terminations against lower set boundaries and structureless parts of fills (Alexander *et al.*, 2001; Cartigny *et al.*, 2014; Fedele *et al.*, 2016; Hofstra *et al.*, 2018; Slooman & Cartigny, 2020). However, the Type B laminasets lack upstream migrating laminae sets, cross-cutting laminasets and structureless components.

Despite similarities to documented combined flow structures, such as convex-up bedforms and

small-scale HCS (Tinterri & Muzzi Magalhaes, 2011; Bell *et al.*, 2018; Hofstra *et al.*, 2018; Tinterri *et al.*, 2022), the Type B laminasets have markedly different textural properties, such as heterolithic foreset laminae/banding, mud-rich trough-fills and low aspect ratios. Type B laminasets therefore likely formed underneath both transitional and combined flow regimes with cohesive forces and rapid deceleration above topography. The transitional flows take on the dynamics of combined flows and thus deposit and rework sediment beds into mixed sandstone-mudstone biconvex ripples and small-scale HLCS laminae/banded sets. Biconvex ripples are therefore interpreted to form under combined TETF and LTPF conditions, and HLCS laminasets and banded sets are interpreted to form under combined UTPF conditions.



Video. 1. Photogrammetric model of an internal levée core section (BAV 2, 66.65–66.79 m, core width: 65 mm). Model highlights the three-dimensional geometry and texture of mixed grain-size hummock-like and swale-like laminasets (HLCS).



Video. 1. Photogrammetric model of an internal levée core section (BAV 2, 73.07–73.45 m, core width: 65 mm). Model highlights the three-dimensional geometry and texture of small-scale hummock-like and swale-like laminasets (HLCS), and their gradual transition from swale-like to hummock-like within laminasets.

BEDFORM SEQUENCES AND DISTRIBUTIONS

The mixed grain-size bedforms of *unidirectional transitional flows* (Type A) and *combined transitional flows* (Type B) stack to form distinct *bedform sequences* (Fig. 11). The observed stratigraphic transitions between the different bedforms are not

mutually exclusive. Some Type A bedforms pass vertically into Type B bedforms and vice versa within a single bedform sequence.

An ideal vertical sequence of Type A bedforms has a sharp or weakly erosional lower boundary overlain by low-angle climbing sand-rich current ripples and mud-rich current ripples at the base, before passing upward through high-angle climbing mud-rich current ripples, LABWs, and sinusoidal laminasets at the top of the sequence, thus supporting deposition from unidirectional transitional flows (Figs 11A and 12A). Type A bedform sequences are between 5 to 30 cm thick, and normally graded from mixed very-fine sand and coarse silt to mudstone (Fig. 12A). The climb angle of constituent laminae progressively increases upward, which corresponds with an upward increase in bedform wavelength and a reduction in bedform amplitude (Fig. 4).

An ideal vertical sequence of Type B bedforms comprises a sharp or weakly erosional lower boundary overlain by biconvex ripples, which passes upward through thick laminasets (40–50 cm) of HLCS, therefore supporting deposition from combined, transitional flows (Fig. 11B; Tinetti, 2011). Laminasets and banded sets of HLCS gradually transition upward from erosionally-based swale-like structures at the base of the set to hummock-like structures towards the top. Throughout the transition, the hummocks become progressively tighter, and the internal laminae become thicker, until they resemble banding (Fig. 12B, Video 2). Locally, HLCS bedforms transition to Type A LABWs and/or sinusoidal laminasets at bed tops (Fig. 12B). The climb angle of constituent laminae progressively increases upward, which relates to an upward increase in wavelength and a reduction in bedform amplitude (Fig. 9). Type B bedform sequences (5–50 cm thick) comprise mixed fine to very-fine sandstone and fine siltstone, which grades normally to mudstone (Fig. 12).

Stratigraphic and palaeogeographical bedform sequence distributions

The thickest Type A bedform sequences are observed in channel margin, proximal internal levée and frontal lobe off-axis environments and contain the most complete set of bedform transitions from mud-rich current ripples through to sinusoidal laminasets (Fig. 12). In sand-prone environments, such as channel margins, Type A bedforms sometimes transition upward from sand-rich current ripples at bed bases. In

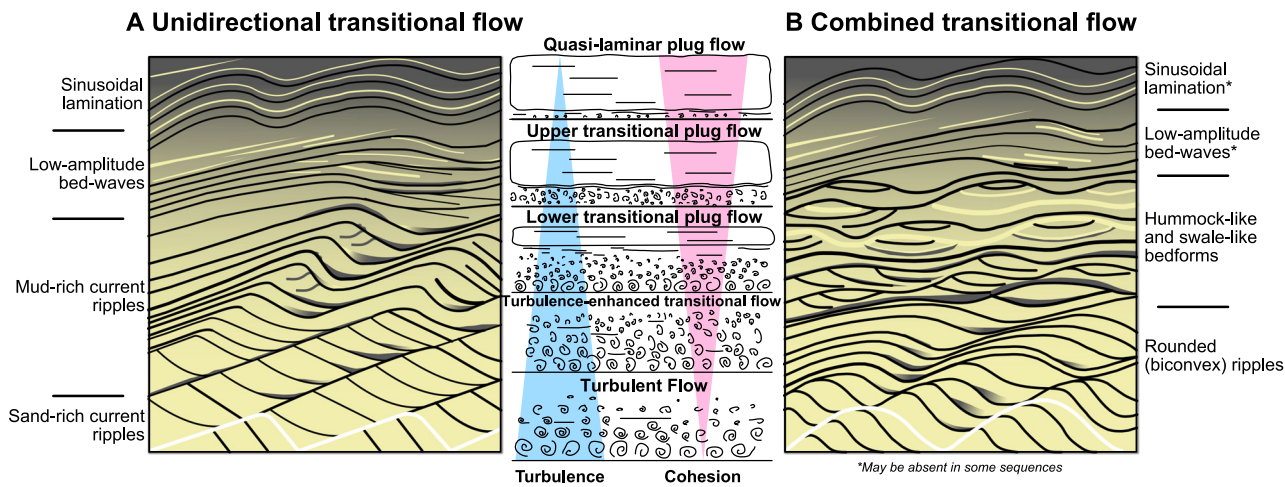


Fig. 11. Schematic model for flow transformation of initially turbulent flows which produce discrete bedform sequences underneath rapidly decelerated cohesive transitional flows in submarine slope settings. (A) Idealized bedform sequence for Type A *unidirectional* transitional flows. (B) Idealized bedform sequence for Type B *combined* transitional flows, adapted from Tinterri (2011, fig. 17B). Indicative transitional flow signatures (*sensu* Baas et al., 2009) are shown for each bedform. White lines at base in (A) and (B) represent initial bedform geometries.

environments away from channel-fills, such as distal internal levées, Type A bedform sequences are much thinner (<10 cm thick), scarcer, and mostly comprise LABWs, sinusoidal laminasets and starved laminae (Fig. 13A). Type B bedform sequences are between 5 to 50 cm thick in proximal internal levée and lobe off-axis environments, while in distal internal levées and intraslope lobe fringes, they are between 2 to 10 cm thick and mainly contain HLCS banded sets and sinusoidal laminasets (Fig. 13B). Type A and B bedform sequences are not observed in sand-prone channel axis environments, or inter-unit mudstones.

Figures 14 and 15 show thickness distributions of the different transitional flow bedform sequences (Type A and Type B) and cohesionless turbulent flow bedforms from the studied core sections. In the Unit C2 internal levée environment (Fig. 14, BAV 2), unidirectional and combined transitional flow bedform sequences comprise 27.4% of the total thickness of the studied core section, with similar proportions of Type A and Type B sequences, as opposed to turbulent flow bedforms (sand-rich current ripples), which comprise 2.5%. Type A bedform sequences are clustered at the top and base of the internal levée section, while Type B bedform sequences are more evenly distributed. In individual beds, Type B bedforms can transition

upward into Type A bedforms, before passing into thicker mudstone units. In the Unit C3 frontal lobe environment (Fig. 14, BAV 1A), transitional flow bedform sequences comprise 62.9% of the total thickness of the core section, and turbulent flow bedforms comprise 15.5%. Type A bedform sequences are most common, with thicker, more complete, sequences observed towards the top of the unit. Type B bedform sequences are the second most common but form the thickest sequences. These tend to cluster at the base of the frontal lobe section before thinning upward.

In the Unit D channel margin and internal levée environments (Fig. 15, BAV 4), unidirectional and combined transitional flow bedforms (Type A and B) comprise 39.4% of the total thickness of the studied core section. Type A bedform sequences are evenly distributed, with some clustering of the thicker beds within channel margins. Conversely, Type B bedform sequences are clustered within internal levée packages, in-between channel-fills. With lateral distance from channel-fills (Fig. 15, BAV 5), the proportion of transitional flow bedforms decreases, although the proportion of Type B bedform sequences increases slightly with respect to Type A sequences and turbulent flow bedforms. Type A sequences are clustered throughout the succession, separated by thick mudstone packages. Type B bedform

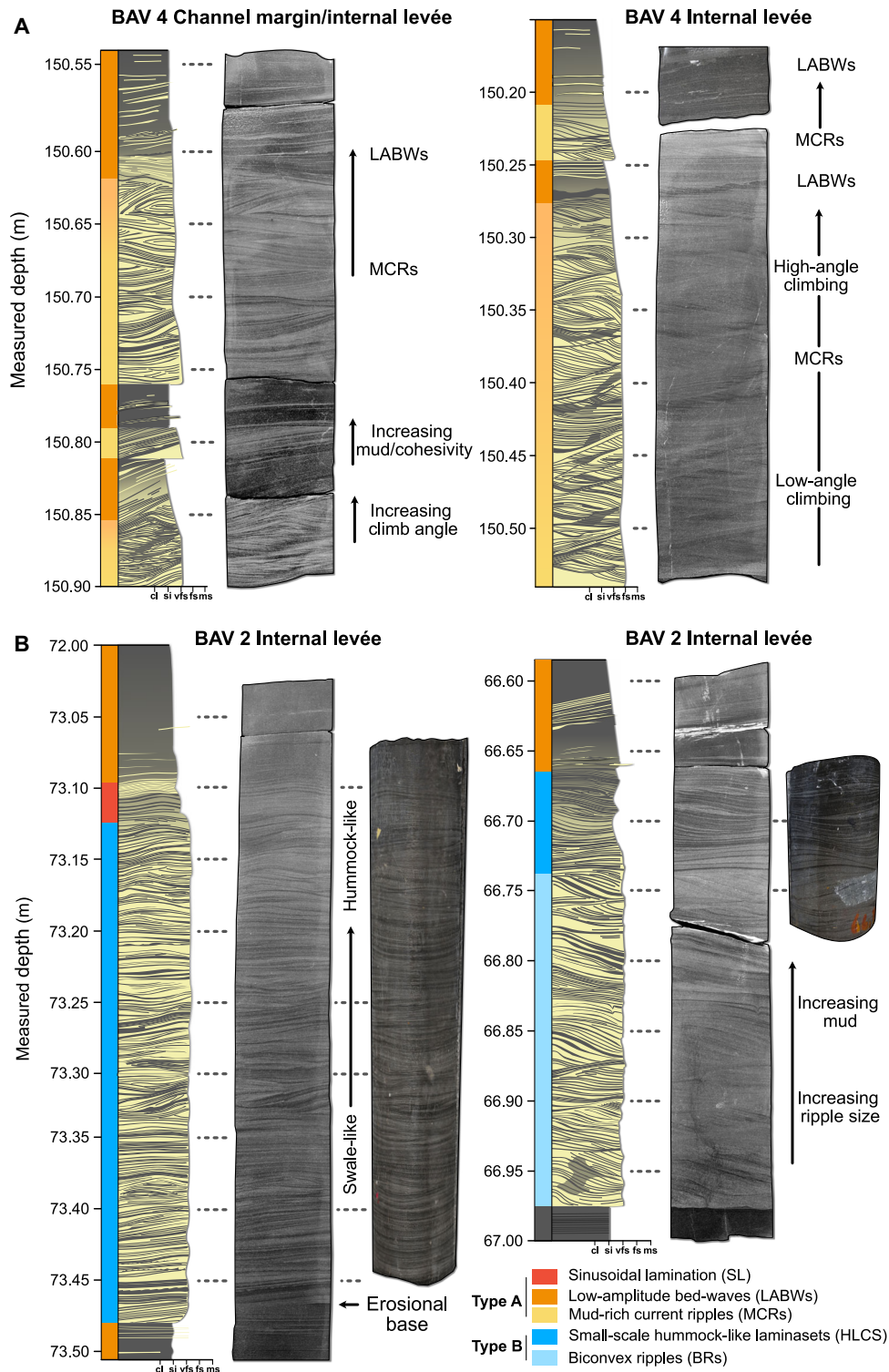


Fig. 12. Representative core logs, high-contrast photographs and three-dimensional photogrammetric scans, which highlight the internal structure and laminaset transitions of: (A) Type A bedform sequences, formed under *unidirectional* transitional flows; and (B) Type B bedform sequences, formed under *combined* transitional flows.

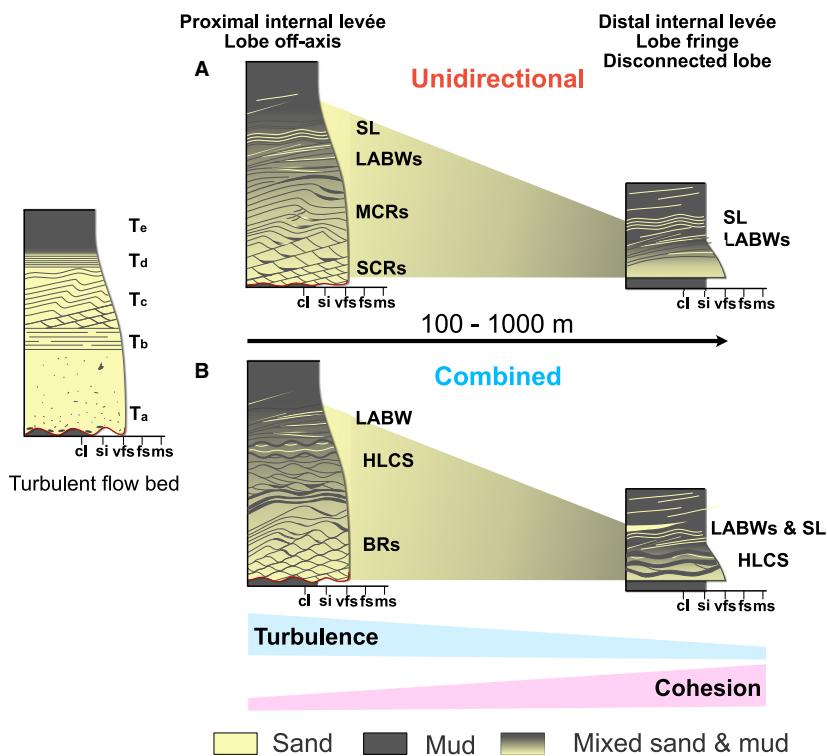


Fig. 13. Conceptual diagram highlighting the lateral variation in bedform sequence character with distance from the site of mud entrainment and/or point of flow deceleration. This schematic is based on observations of Unit D bedforms between boreholes BAV 4 and BAV 5. (A) Lateral variation of unidirectional transitional flow bedform sequences (Type A). (B) Lateral variation of combined transitional flow bedform sequences (Type B). A typical sequence of turbulent flow bedforms is shown for comparison. BRs, biconvex ripples; HLCS, hummock-like cross-stratification; LABWs, low-amplitude bed-waves; MCRs, mud-rich current ripples; SCRs, sand-rich current ripples; SL, sinusoidal lamination.

sequences are predominantly at the base of the succession, stratigraphically above laterally stacked channel-fills (Fig. 15, BAV 5). Few bedforms are present in the distal internal levée, with thin Type A bedform sequences, isolated within thick mudstone packages.

At outcrop sections, the full extent of unidirectional and combined transitional flow bedform sequences are observed. At the disconnected lobe section (Unit A/B), Type A sequences (10–50 cm thick) are most common, containing low to high angle mud-rich current ripples, which gradually thin and lengthen upward into LABWs (Fig. 4A). Type B bedform sequences are thinner (5–20 cm), and observed at the margins of the disconnected lobe, with sub-symmetrical rounded profiles and internal swale-like and hummock-like laminasets (Fig. 9A). At the intraslope lobe section of Unit E, Type B bedform sequences thicken upward (up to 2 m thick). The Type B bedforms have clear, rounded swale and hummock-like planform surfaces, with palaeocurrent directions that appear to deviate from the regional flow direction (Fig. 6C), suggesting flow deflection. The Type B sequences tend to transition upward from Type A sequences, which occur in thinner bedded mud-rich packages (<50 cm thick), interspersed between the Type B bedform sequences (Fig. 6).

DISCUSSION

Flow transformations in submarine slope settings

The bedform sequences described here are interpreted as a product of flow transformation between the transitional flow phases from turbulent to laminar states (Fisher, 1983; Baas *et al.*, 2021a). Bedform type is inferred to be strongly influenced by the rate of flow deceleration (Sumner *et al.*, 2009), the balance of cohesive and turbulent forces (Baas *et al.*, 2009, 2011, 2016), and topography (Tinterri, 2011).

Type A bedform sequences record temporal unidirectional flow transformation (Fig. 11A). In submarine slope environments, flow transformation is likely triggered by rapid deceleration of flows that are stripped or overspill the confinement of channels (e.g. Piper & Normark, 1983; Hiscott *et al.*, 1997; Peakall *et al.*, 2000a), or through loss of momentum due to flow expansion at channel mouths (e.g. Mutti & Normark, 1987, 1991; Spychala *et al.*, 2020; Hodgson *et al.*, 2022). The upward transition from sand-rich current ripples to mud-rich current ripples in channel margins likely records the initial phase of transformation from a fully turbulent, non-cohesive flow to TETF or LTPF conditions (*sensu* Baas *et al.*, 2009).

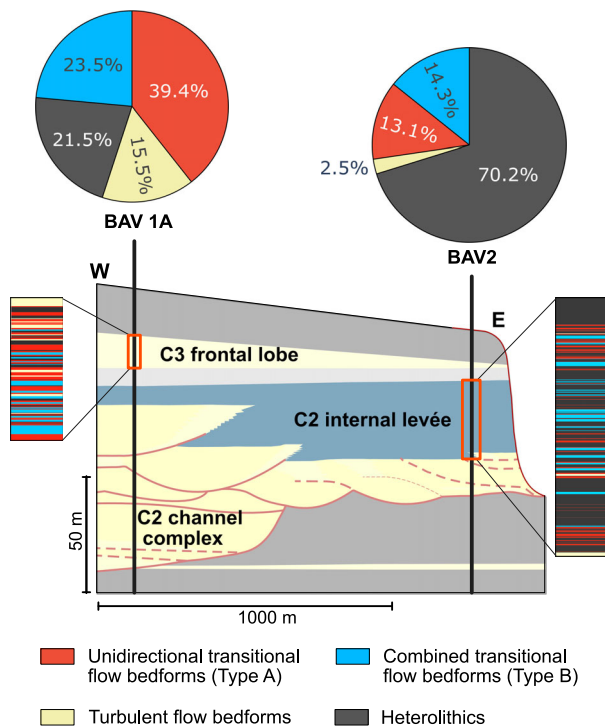


Fig. 14. Distribution of unidirectional and combined bedform sequences from subunits C2 and C3, interpreted from boreholes BAV 1A and BAV 2. Pie charts show the thickness proportion of each bedform sequence for each studied core section. Percentage values are rounded to one decimal place. Refer to Fig. 1C for depositional environments. Palaeoflow direction is into the page.

The rapidly decelerating flow may become more cohesive due to entrainment of mud-prone substrates on the slope (e.g. Brooks *et al.*, 2018) and/or

flow partitioning, where the upper part of the flow overflows the channel and becomes enriched in mud, as the denser, sand-rich fraction of the flow remains confined to the channel (Piper & Normark, 1983; Peakall *et al.*, 2000a,b; Hansen *et al.*, 2015). Both factors would result in an early phase of near-bed flow turbulence enhancement (e.g. Baas *et al.*, 2021a), which drives erosion on lee sides of mud-rich current ripples, thus promoting the increases in bedform amplitude and formation of backset laminae (Fig. 3E and F). Further flow deceleration and increases in suspended mud concentration (as coarser grains drop out of suspension) would significantly dampen turbulence and result in transformation to UTPF conditions (*sensu* Baas *et al.*, 2009). This causes the observed reduction in bedform amplitude and increases in wavelength, thus generating LABWs (Fig. 4A). At this point, the flow is highly decelerated and cohesive, which results in higher climb angles and rapid aggradation, as indicated by the sinusoidal laminasets at bed tops. The apparent lengthening of the sinusoidal laminasets as the set climbs in some laminasets (Fig. 7C) might suggest further flow transformation through turbulence attenuation by cohesive clay in the flow (Baas *et al.*, 2021a). Eventually, traction is fully suppressed and bedforms no longer form, as indicated by the ‘starved lamination’ texture and packages of faintly bedded mudstones (Table 1, F5), as the flow transitions to QLPF conditions.

Soft-sediment deformation expressed by the kinked foresets, loaded mud foreset laminae and erosion in the troughs of some laminasets (Fig. 3H and I), suggests that flow transformation through the Type A bedform sequence occurred rapidly.

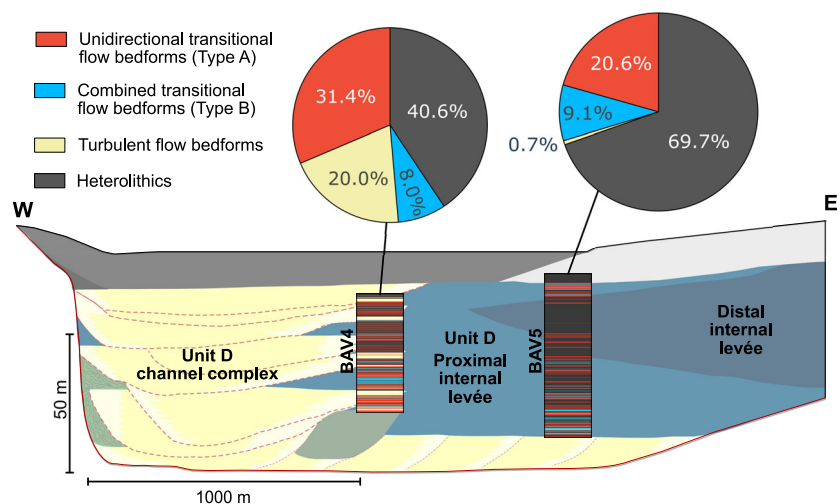


Fig. 15. Distribution of bedform sequences across Unit D, interpreted from boreholes BAV 4 and BAV 5. Pie charts show the thickness proportion of each bedform sequence for each studied core section. Percentage values are rounded to one decimal place. Refer to Fig. 1C for depositional environments. Palaeoflow direction is into the page.

Comparisons to quantitative analysis of climb angle and laminae size of a climbing ripple co-set from Baas *et al.* (2021a), suggest that a single bedform sequence was likely deposited over a period of minutes to tens of minutes. The stacking of laminasets within Type A bedform sequences are similar to the observations of Baas *et al.* (2021a), although the observations herein demonstrate flow transformation from mud-rich current ripples all the way to LABWs and sinusoidal laminasets, rather than a more restricted transition to relict large ripples (cf. Baas *et al.*, 2021a), across the complete range of transitional flow types.

Type B bedform sequences similarly indicate temporal transformation through the transitional flow types, with the addition of a combined flow component (e.g. Dumas *et al.*, 2005, Fig. 11B). In submarine slope settings, combined flows most likely occur from flow reflection, deflection or ponding processes against topography (e.g. Pickering & Hiscott, 1985; Haughton, 1994; Hofstra *et al.*, 2018). Initially, flows that interact with topography might generate an oscillatory component that combines with a strong unidirectional component at 180° to the flow direction (Yokokawa *et al.*, 1995). Here, the bedforms are characterized by the biconvex ripples. The subsequent upward passage into small-scale HLCS laminasets (Fig. 12B), coupled with the upward tightening and thickening of the mud-rich hummock-like bands could represent a relative increase in the oscillatory component associated with internal waves produced by flow reflection and ponding processes (Patacci *et al.*, 2015; Howlett *et al.*, 2019; Tinterri *et al.*, 2022), or through turbulence attenuation from increases in flow cohesion (e.g. Baas *et al.*, 2016; Tinterri *et al.*, 2022). A combination of both processes is likely, such that the flow transforms through the same transitional flow types as with Type A bedform sequences, from TETF–LTPF conditions as expressed by biconvex ripples, to LTPF–UTPF conditions as indicated by the HLCS laminasets (Fig. 11B). The transition from HLCS into LABWs sometimes observed at bed tops, suggests that further flow transformation to UTPF or QLPF conditions occurs in these cases (Baas *et al.*, 2021a).

The absence of the upper LABW and sinusoidal lamination section at the top of some Type B sequences, in contrast to Type A sequences, suggests that some of the flows do not reach the transition between UTPF and QLPF flows; perhaps because of additional turbulence developed during interaction with topography, and the generation of an oscillatory component. However, where present, the dominance of unidirectional flow in

the LABWs and sinusoidal lamination suggests that the high cohesion of these flows shuts down the topographically-induced oscillatory flow component (e.g. Tinterri *et al.*, 2022). Mechanistically, this absence of an oscillatory component may result from the shielding of the more fluidal layers towards the base of the flow, where bedforms develop, by the overlying high-strength cohesive plug at the transition between UTPF and QLPF flows (Baas *et al.*, 2009).

The continuous passage through the different Type B bedforms in a single bed also support greater affinity with reflected and deflected flow transformations from topographic interactions than unidirectional supercritical flows (Hofstra *et al.*, 2018). The upward transition from Type A to Type B bedform sequences (Fig. 6) in some sections is interpreted to record the temporal transformation from a unidirectional transitional flow to a combined transitional flow as the flow decelerated and thinned and became increasingly susceptible to topographic influence (cf. Kneller & Buckee, 2000).

Lateral changes in bedform sequence appearance, i.e. from proximal to distal internal levée (Fig. 13), support the spatial transformation of flows that escape channel confinement and transform from turbulent to laminar as they run out, decelerate and potentially entrain additional cohesive mud. In proximal areas, transitional flow bedform sequences are typically thick and comprise the full range of Type A and Type B bedform transitions, whereas in distal areas, bedform sequences are much thinner, muddier, and only contain LABWs and sinusoidal laminasets in Type A sequences, or HLCS banded sets, LABWs and sinusoidal laminasets in Type B sequences (Fig. 13).

Using transitional flow bedforms to interpret the geological record

Both unidirectional and combined transitional flow bedform sequences (Types A and B) are more common than the deposits of cohesionless, turbulent flows (for example, sand-rich current ripples) observed in this study. This observation holds true across the studied depositional environments of the Laingsburg depocentre (Figs 14 and 15), thus demonstrating that submarine slope systems are conducive to flow transformations. Therefore, unidirectional and combined transitional flow bedform sequences are likely an important component in other slope successions, where mud is available to be entrained and seabed topography is present. Transitional flow bedform sequences should therefore be

used to support depositional environment interpretations on submarine slopes. For instance, Type A bedform sequences are predicted to develop in environments where unidirectional flows rapidly decelerate and have elevated proportions of cohesive mud, while Type B bedform sequences are predicted to develop where transitional flows interact with seabed topography or confining slope surfaces (Fig. 16). These observations also suggest that existing models of mixed grain-size bedform development in slope settings that only invoke non-cohesive flow processes (e.g. Stow & Shanmugam, 1980; Shanmugam *et al.*, 1993a; Morris *et al.*, 2016), must be re-evaluated.

Slope channel-levée complexes (Units D and C2)

The thickest, most complete Type A bedform sequences are observed in the channel margins of Unit D (Fig. 15, BAV 4). The presence of such bedforms in this setting could support flow separation at the inner bends of channels, as slightly lower rates of deceleration permit higher aggradation rates and more sustained periods of traction (e.g. Allen, 1982; Southard & Boguchwal, 1990; Sumner *et al.*, 2008), and therefore deposit beds with thicker bedform sequences. Mud is commonly deposited in channels during periods of reduced activity, or by channel margin collapse, thereby forming the substrate for flows to entrain mud and sufficiently dampen turbulence to contribute to the upward transition from sand-rich current ripples to mud-rich current ripples.

In the Unit D and C2 internal levées, Type A bedform sequences represent unidirectional flows that experienced rapid decrease in confinement as (parts of) the flow escaped the channels (Fig. 16B). Unidirectional flow transformation may have been enhanced by entrainment of cohesive sediment, because internal levées are typically mud-prone environments (Kane & Hodgson, 2011). In the proximal internal levée (Fig. 15, BAV 4), Type A bedform sequences are thicker and contain more complete bedform transitions from mud-rich current ripples to LABWs than those observed in the distal internal levée (Fig. 15, BAV 5). This lateral change in bedform appearance with distance from channel-fills points to lateral unidirectional flow transformation across the internal levée (Fig. 13), as flows escape channel confinement and decelerate, but remain within the larger scale confines of the valley entrenchment (Fig. 16B). These observations likely indicate flow run out distances, for instance, regarding Unit D, transitional flows

appear to run out and transform over 1 to 2 km. Such observations are broadly comparable to those made from fan fringe to distal fringe environments of basin fans (2–3 km; Baker & Baas, 2020). Similar lateral trends in bedform sequence appearance are also observed in the Unit D external levée, where high magnitude flows escaped the larger scale confines of the entrenched valley and decelerated down the external levée flanks (Fig. 4D).

The distinct clusters of Type A bedforms in the Unit D distal internal levée adjacent to aggradationally stacked channel-fills (Fig. 15, BAV 5) could record either the lateral extent of overspilling unidirectional transitional flows, or the periodic downstream migration of an outer channel bend, captured from a downstream inner bend position, where there is enhanced flow stripping (Peakall *et al.*, 2000a). The upward decrease in the number and thickness of Type A bedform sequences in this section (Fig. 15) could represent increased channel relief with time (Hiscott *et al.*, 1997; Pirmez & Imran, 2003), or alternatively indicate decreases in the magnitude of SGFs as the system aggraded (Kneller, 2003).

Type B bedform sequences are mainly observed in the internal levées (Figs 14 and 15), where flows transition as they pass over mud-prone substrate and interact with erosional and depositional relief (Fig. 16B). In some Unit D sections, Type B sequences are composed of thin laminasets of biconvex ripples that pass into Type A LABWs with thick mudstone caps (Fig. 12). This suggests flows that overspilled the channel, deflected off valley topography and decelerated rapidly. The mudstone caps suggest ponded deposition in topographic lows (e.g. Pickering & Hiscott, 1985; Haughton, 1994) on the internal levée, which could have multiple origins, such as mass transport relief or abandoned channel bends.

In the Unit D distal internal levée, Type B bedform sequences are clustered at the base of the section and thin upward (Fig. 15, BAV 5). This points to decreasing flow interactions with remnant topography in the degraded landscape from the westward migration of the Unit D channel complex, during the initial stages of internal levée aggradation. This is also likely coupled with reflection and deflection off slope valley relief, which additionally generated combined transitional flows. The upward decrease in the thickness of Type B bedform sequences and increase in Type A bedforms suggests that flows were then not able to interact with the margins of the slope valley, which supports a decrease in flow magnitude, and/or increases in channel relief during system

aggradation, or further migration of the channel complex away from the BAV 5 intersection.

In Unit C2, the location of the eastern confining external levée is unconstrained, because Unit D incised and removed the external levée crest area (Morris *et al.*, 2016). However, the even stratigraphic distribution of Type B bedform sequences and thick laminasets of biconvex ripples and HLCS in the internal levée section (Fig. 14, BAV 2), suggest that combined transitional flows were repeatedly generated from deflection off the inner external levée (Fig. 12B). This observation implies that the eastern inner external levée of Unit C2 might have been close to the BAV 2 intersection.

Intraslope lobe complexes (Units A/B, C3 and E)

Both transitional flow bedform sequence types are observed in frontal, disconnected and intraslope lobe environments. In Unit A/B (disconnected lobe), Type A bedform sequences transition upward from mud-rich current ripples to LABWs (Fig. 4A) and stack to form thin, discontinuous lobe sandstones fed by multiple, incipient channels (Brooks *et al.*, 2018). Increases in flow cohesion (likely from entrainment of the thick underlying mudstones), and rapid flow deceleration associated with decreased gradient at the base-of-slope, caused turbulence damping and deposition of the Type A bedform sequences (Fig. 16A). The presence of Type B bedform sequences comprising laminasets of biconvex ripples and HLCS at the bases and margins of the disconnected lobes (Fig. 8D) suggest the presence of topographic relief, which previously had been invoked based only on planform patterns (Brooks *et al.*, 2018).

In Unit C3, the frontal lobe complex received sediment from defined flow pathways (Morris *et al.*, 2014b; Brooks *et al.*, 2018). Hence, the development of Type A bedforms was likely triggered by rapid flow expansion and deceleration at channel mouths (e.g. Mutti & Normark, 1987, 1991; Fig. 16A). The presence of Type A bedform

sequences can therefore be used to support interpretations of channel-lobe transition zones (CLTZs) associated with abrupt changes in slope gradient (e.g. Hofstra *et al.*, 2018), or at channel mouth expansion zones (CMEZs, Hodgson *et al.*, 2022), where flows are susceptible to rapid deceleration and entrainment of mud to increase cohesive forces. The upward thickening of Type A bedform sequences possibly represents the lateral offset pattern of the C3 frontal lobe complex (Morris *et al.*, 2014b), where each successive lobe deposit was compensationally stacked 'towards' the core section (e.g. Prélat *et al.*, 2009).

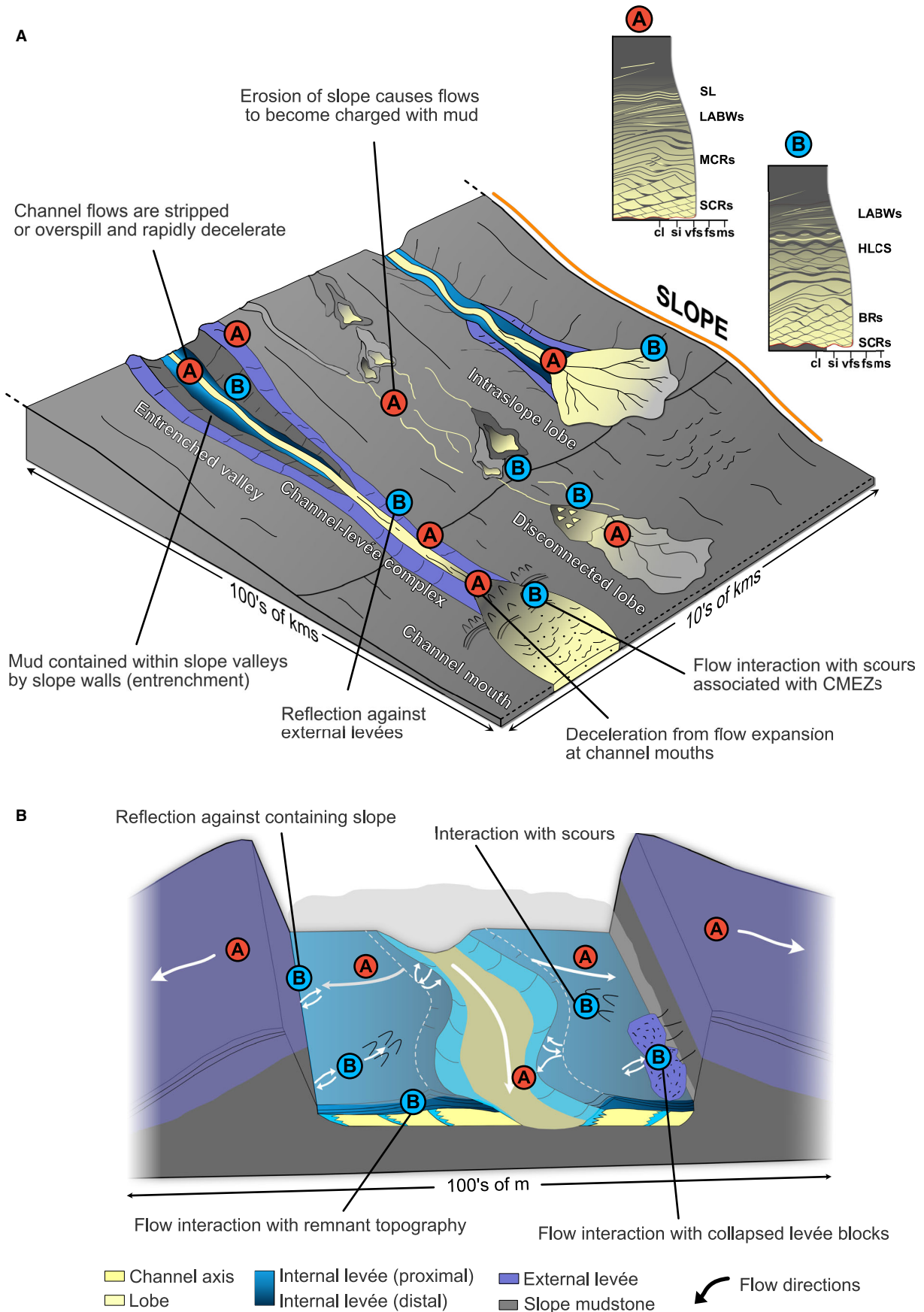
Type B bedforms are the oldest deposits of the C3 frontal lobe complex and form thick bedform sequences that contain biconvex ripples and HLCS banded sets (Figs 9E and 10E) clustered at the base of the section (Fig. 14), associated with frontal lobe off-axis to fringe environments (Morris *et al.*, 2014b). Here, flows likely deflected off both erosional and depositional relief, such as scours and sediment waves to set up a combined transitional flow, thus supporting interpretations of a channel mouth transition zone, where these features are common (Fig. 15; Hodgson *et al.*, 2022).

In the Unit E intraslope lobe section, Type B bedform sequences transition upward from Type A sequences and appear to thicken upward (Fig. 6). This is likely a record of changing flow magnitudes, where the thinner Type A sequences record smaller flows that were unaffected by the confining intraslope topography, and only represent flows that decelerated from decreases in slope gradient. Conversely, the Type B bedform sequences are records of larger magnitude flows that were able to 'feel' the intraslope confining topography, and thus set up a combined flow.

Distinguishing transitional flow bedforms from the deposits of other ocean currents

Differentiating the deposits of turbulence-modulated transitional flow bedforms from other ocean currents, such as along-slope bottom

Fig. 16. (A) Conceptual diagram of a slope setting showing the locations where transitional flow bedforms are expected to form. Unidirectional transitional flow bedforms (Type A) are expected to form close to sites of rapid deceleration and sites of erosion into mudstone substrates. Combined transitional flow bedforms (Type B) are expected to form near sites of topography. (B) Zoomed-in section of a slope valley setting (for example, Unit D), where sites of topography are expected to form combined transitional flow beds (Type B). Grain-size range of bedform Types A and B will vary as a function of sediment input. BRs, biconvex ripples; CMEZ, channel mouth expansion zone (*sensu* Hodgson *et al.*, 2022); HLCS, hummock-like cross-stratification; LABWs, low-amplitude bed-waves; MCRs, mud-rich current ripples; SCRs, sand-rich current ripples; SL, sinusoidal lamination.



currents (i.e. contour currents), in the stratigraphic record needs to be considered. This is challenging because bottom currents also deposit and rework sediment on continental slopes (e.g. Rebesco *et al.*, 2014; de Weger *et al.*, 2020; de Castro *et al.*, 2021; Fuhrmann *et al.*, 2022; Rodrigues *et al.*, 2022), and sediment gravity flows can be affected by bottom current processes during and after deposition (e.g. Miramontes *et al.*, 2020).

Characteristics thought to be diagnostic criteria of bottom current deposits (i.e. contourites, or bottom current reworked sands), include sequences composed of rhythmically layered, thin-bedded to laminated sand and mud, low-angle cross-bedding, starved ripples, sharp to gradational contacts, and high levels of bioturbation (Shanmugam *et al.*, 1993a,b; Stow & Smillie, 2020). More recent work interprets ‘mud-rich contourites’ (Rodrigues *et al.*, 2022), which are likewise described as repetitive sequences of cross to parallel-laminated, fine to coarse-silt laminae that grade upward into silty clay. Internally, these deposits include mud-rich ripples, starved ripples and irregular wavy laminations (Rodrigues *et al.*, 2022, facies d).

This study proposes that these mud-rich bedforms, previously interpreted as contourites (Rodrigues *et al.*, 2022), are in fact Type A bedform sequences, indicated by transitions between mud-rich current ripples, LABWs and sinusoidal lamination. Therefore, they are more readily explained by transformations of sediment gravity flows. Critically, these mixed grain-size and mud-rich bedforms are hard to reconcile with a bottom current interpretation because persistent bottom currents are shown to have particularly low sediment concentrations, in the order of 20 to 500 µg/L (Zhao *et al.*, 2015; Gardner *et al.*, 2018; Stow & Smillie, 2020), and thus cannot account for the appreciable amount of mud observed in laminates, or their high angles of climb. Furthermore, the segregation of grain sizes and upward increases in mud content within bedforms is difficult to reconcile with long-lived bottom currents, because they should winnow their own deposits, producing clean bedforms, for example, clean sand current ripples (Baas *et al.*, 2013; de Castro *et al.*, 2020). The process of winnowing can be reduced, or prevented, under cohesive flow conditions (Baas *et al.*, 2013); however, this is unlikely to be the case under bottom currents, given their low sediment concentrations (Zhao *et al.*, 2015; Gardner *et al.*, 2018).

The winnowing of clay from mixed sand–mud is a highly efficient process, therefore the removal of mud from bedforms can be particularly rapid (Baas *et al.*, 2013). Accordingly, the preservation

of alternating sand-laminae and mud-laminae from sustained bottom currents would require especially rapid sediment burial. However, measured accumulation rates of bottom current deposits of ca 0.95 g/m²/day (Zhao *et al.*, 2015), suggest that this is also unlikely. Malarkey *et al.* (2015) demonstrated that the addition of cohesive biological components slows the removal of fines by an order of magnitude, but given the long-lived nature of contourite systems, it is likely that this makes little difference to the winnowing process. Bottom currents are also far steadier in their temporal velocity pattern compared to sediment gravity flows (e.g. Zhao *et al.*, 2015; Miramontes *et al.*, 2019; Fuhrmann *et al.*, 2020), which is hard to reconcile with the development of mixed-grain size bedform sequences, shown to form from rapid flow deceleration and transformation on the order of minutes to tens of minutes (Baas *et al.*, 2021a), as opposed to weeks to months (Zhao *et al.*, 2015; Miramontes *et al.*, 2019). Caution is therefore advised in the use of mixed grain-size bedforms as a diagnostic criterion for contourites, and that flow transformations from mud-rich flows are a more readily explainable sedimentary process mechanism for their formation.

It should be acknowledged that bottom currents may rework deposits of transitional flows; for instance, the streaky, ‘starved lamination’ associated with LABW deposition (Fig. 5A) is documented in other studies where it has been interpreted as dilute sediment gravity flow deposits reworked by intermittent bottom currents (de Castro *et al.*, 2020, 2021; Fuhrmann *et al.*, 2022). However, these structures are expected to be accompanied by upward coarsening and better sorting due to winnowing, but this is not seen in the examples documented in this study. It is therefore concluded that the influence of bottom currents on the development of mixed grain-size bedforms in the Laingsburg depocentre is unlikely, particularly as the Karoo Basin was not an ocean-facing system at the time of deposition (Tankard *et al.*, 2009).

The original interpretation of mixed grain-size bedforms as a diagnostic criterion for bottom currents and bottom current reworked sands, was postulated for deposits in the Ewing Bank and Garden Banks areas of the US Gulf of Mexico (Shanmugam *et al.*, 1993a,b). The rationale was three-fold: (i) mixed grain-size bedforms did “not conform to conventional deep-marine facies model dominated by turbidites” (Shanmugam *et al.*, 1993b); (ii) traction and cross-bedding were more likely to occur under clear water flows such as bottom currents than under sediment-charged turbidity

currents; and (iii) an assumption was made that the loop current was present at the depth and time of deposition (Shanmugam *et al.*, 1993a,b). Turbidity currents are well-known to exhibit a wide range of tractional structures (e.g. Bouma, 1962; Sanders, 1965; Walker, 1967; Mutti, 1992; Jobe *et al.*, 2012; Fedele *et al.*, 2016). Furthermore, new models of sediment gravity currents have moved beyond the concepts of cohesionless turbidity currents that were prevalent in the early 1990s. These new models are based on physical experiments and outcrop observations, many of the latter in basins too small for bottom currents (e.g. Baas *et al.*, 2011, 2016, 2021a,b; Baker & Baas, 2020). Herein this study has shown for the first time, in a well-constrained palaeogeographical setting, that mixed grain-size bedforms are characteristic of mud-rich sediment gravity flows on submarine slopes. Given this new knowledge, the Gulf of Mexico examples described by Shanmugam *et al.* (1993a,b), can now be reassessed as the product of mud-rich sediment gravity flows in down-slope systems. Therefore, this reinterpretation implies that deposition was too rapid for later reworking by a bottom current, and/or that the bottom current was not present at the site of deposition (Brunner, 1982; Arellano-Torres *et al.*, 2023).

CONCLUSIONS

Mixed grain-size bedforms were examined using core and outcrop data from a range of well-constrained submarine slope environments from the Permian Laingsburg depocentre, South Africa. This study reveals two distinct bedform sequences comprised of different mixed grain-size bedforms that represent progressive variations in flow properties. Type A bedform sequences consist of mixed sandstone–mudstone asymmetrical mud-rich current ripples and low-amplitude bed-waves that comprise alternating concave and planar sandstone–mudstone foresets, and aggradational mixed sinusoidal laminasets. Type B bedform sequences consist of sub-symmetrical rounded, biconvex ripples with sigmoidal-shaped foresets and small-scale swale-like and hummock-like cross-stratification that comprise alternate sandstone–mudstone banding. Both bedform sequences are interpreted as the product of transitional flows, where constituent bedforms and their distribution are controlled by the balance of cohesive and turbulent forces and the rate of flow deceleration. Type A bedforms are interpreted to form under unidirectional transitional flows, while

Type B bedforms are records of flows that interacted with topography to form combined transitional flows. Furthermore, the characteristic upward and lateral transitions between different bedforms point to progressive spatio-temporal transformations in flow properties and their topographic interactions, and, as such, these bedform sequences can be used to support interpretations of depositional environment. Both bedform sequences are common and represent between 27 to 63% by stratigraphic thickness of the studied slope successions, which include channel-margin, internal-levée and external-levée, intraslope and disconnected lobe environments. They are typically situated close to sites of erosion into mud-prone substrates, abrupt losses in confinement, and/or changes in slope gradient. Type B bedform sequences are further associated with flow deflection against erosional and depositional relief, such as scours or sediment waves, which are common in incised slope valleys and channel mouth settings. They can therefore be used as a new criterion to indicate flow confinement.

These mixed grain-size bedforms and their sequences are the first documented examples of flow transformations from proximal settings and show that transitional flow behaviour is not restricted to the fringes of sedimentary systems. These new insights provide an opportunity to re-evaluate existing process models for many other mixed and mud-prone settings with inherited topography, including deep-water post-rift settings, to account for transitional flow behaviour and their topographic interactions. Care is needed in the distinction of transitional flow bedforms from bottom current deposits. While mixed grain-size bedforms have been considered a diagnostic criterion for bottom currents and bottom current reworked sands for the past 30 years, it can be argued that the field observations herein, and the process mechanics involved in mixed grain-size bedform deposition, do not support a bottom current interpretation. Instead, mixed grain-size bedforms more likely represent the products of unidirectional and combined, mud-rich transitional sediment gravity flows.

ACKNOWLEDGEMENTS

The SLOPE 5 consortium (BP, Aker BP, CNOOC International, Hess, Murphy, Neptune Energy, Petrobras, Vår Energi, Wintershall DEA and Woodside) are thanked for their financial support. We

would like to thank Associate Editor Dr Lawrence Amy, Reviewer Prof. Roberto Tinterri and two anonymous reviewers for their detailed and helpful comments that greatly improved the manuscript.

CONFLICT OF INTEREST STATEMENT

The authors have no conflict of interest to declare.

DATA AVAILABILITY STATEMENT

The data that support the findings of this study are available from the corresponding author upon reasonable request.

REFERENCES

- Alexander, J., Bridge, J.S., Cheel, R.J. and Leclair, S.F. (2001) Bedforms and associated sedimentary structures formed under supercritical water flows over aggrading sand beds. *Sedimentology*, **48**, 133–152.
- Allen, J.R.L. (1968) *Current Ripples: Their Relation to Patterns of Water and Sediment Motion*, p. 433. North-Holland Publishing Company, Amsterdam.
- Allen, J.R.L. (1971) Instantaneous sediment deposition rates deduced from climbing-ripple cross-lamination. *J. Geol. Soc. London*, **127**, 553–561.
- Allen, J.R.L. (1973) A classification of climbing-ripple cross-lamination. *J. Geol. Soc. London*, **129**, 537–541.
- Allen, J.R.L. (1982) *Sedimentary Structures, their Character and Physical Basis*, Volumes 1, 2, 593 pp, 663 pp. Elsevier, Amsterdam.
- Arellano-Torres, E., Amezcua-Montiel, A. and Casa-Ortiz, A. (2023) The loop current circulation over the MIS9 to MIS5 based on planktonic foraminifera assemblages from the Gulf of Mexico. *Paleoceanogr Paleoclimatol*, **38**, e2022PA004568.
- Arnott, R.W. and Southard, J.B. (1990) Exploratory flow-duct experiments on combined-flow bed configurations, and some implications for interpreting storm-event stratification. *J. Sed. Res.*, **60**, 211–219.
- Ashley, G.M., Southard, J.B. and Boothroyd, J.C. (1982) Deposition of climbing-ripple beds: a flume simulation. *Sedimentology*, **29**, 67–79.
- Baas, J.H. and Best, J.L. (2002) Turbulence modulation in clay-rich sediment-laden flows and some implications for sediment deposition. *J. Sed. Res.*, **72**, 336–340.
- Baas, J.H. and Best, J.L. (2008) The dynamics of turbulent, transitional and laminar clay-laden flow over a fixed current ripple. *Sedimentology*, **55**, 635–666.
- Baas, J.H. and De Koning, H. (1995) Washed-out ripples; their equilibrium dimensions, migration rate, and relation to suspended-sediment concentration in very fine sand. *J. Sed. Res.*, **65**, 431–435.
- Baas, J.H., Best, J.L., Peakall, J. and Wang, M. (2009) A phase diagram for turbulent, transitional, and laminar clay suspension flows. *J. Sed. Res.*, **79**, 162–183.
- Baas, J.H., Best, J.L. and Peakall, J. (2011) Depositional processes, bedform development and hybrid bed formation in rapidly decelerated cohesive (mud-sand) sediment flows. *Sedimentology*, **58**, 1953–1987.
- Baas, J.H., Davies, A.G. and Malarkey, J. (2013) Bedform development in mixed sand–mud: the contrasting role of cohesive forces in flow and bed. *Geomorphology*, **182**, 19–32.
- Baas, J.H., Best, J.L. and Peakall, J. (2016) Predicting bedforms and primary current stratification in cohesive mixtures of mud and sand. *J. Geol. Soc. London*, **173**, 12–45.
- Baas, J.H., Best, J.L. and Peakall, J. (2021a) Rapid gravity flow transformation revealed in a single climbing ripple. *Geology*, **49**, 493–497.
- Baas, J.H., Tracey, N.D. and Peakall, J. (2021b) Sole marks reveal deep-marine depositional process and environment: Implications for flow transformation and hybrid-event-bed models. *J. Sed. Res.*, **91**, 986–1009.
- Baker, M.L. and Baas, J.H. (2020) Mixed sand–mud bedforms produced by transient turbulent flows in the fringe of submarine fans: Indicators of flow transformation. *Sedimentology*, **67**, 2645–2671.
- Baker, M.L., Baas, J.H., Malarkey, J., Jacinto, R.S., Craig, M.J., Kane, I.A. and Barker, S. (2017) The effect of clay type on the properties of cohesive sediment gravity flows and their deposits. *J. Sed. Res.*, **87**, 1176–1195.
- Bell, D., Stevenson, C.J., Kane, I.A., Hodgson, D.M. and Poyatos-Moré, M. (2018) Topographic controls on the development of contemporaneous but contrasting basin-floor depositional architectures. *J. Sed. Res.*, **88**, 1166–1189.
- Best, J.L. and Bridge, J.S. (1992) The morphology and dynamics of low amplitude bedwaves upon upper stage plane beds and the preservation of planar laminae. *Sedimentology*, **39**, 737–752.
- Blewett, S.C.J. and Phillips, D. (2016) An overview of Cape Fold Belt geochronology: Implications for sediment provenance and the timing of orogenesis. In: *Origin and Evolution of the Cape Mountains and Karoo Basin* (Eds Linol, B. and de Wit, M.J.), pp. 45–55. Springer, Cham.
- Boulestix, K., Poyatos-Moré, M., Flint, S.S., Hodgson, D.M., Taylor, K.G. and Brunt, R.L. (2022) Sedimentologic and stratigraphic criteria to distinguish between basin-floor and slope mudstones: Implications for the delivery of mud to deep-water environments. *Depositional Record*, **8**, 958–988.
- Bouma, A.H. (1962) *Sedimentology of some Flysch Deposits: A Graphic Approach to Facies Interpretation*, p. 168. Elsevier Pub. Co., Amsterdam.
- Bridge, J.S. and Best, J.L. (1988) Flow, sediment transport and bedform dynamics over the transition from dunes to upper-stage plane beds: implications for the formation of planar laminae. *Sedimentology*, **35**, 753–763.
- Brooks, H.L., Hodgson, D.M., Brunt, R.L., Peakall, J., Poyatos-Moré, M. and Flint, S.S. (2018) Disconnected submarine lobes as a record of stepped slope evolution over multiple sea-level cycles. *Geosphere*, **14**, 1753–1779.
- Brooks, H.L., Ito, M., Zuchuat, V., Peakall, J. and Hodgson, D.M. (2022) Channel-lobe transition zone development in tectonically active settings: Implications for hybrid bed development. *Depositional Record*, **8**, 829–868.
- Brunner, C.A. (1982) Paleogeography of surface waters in the Gulf of Mexico during the late quaternary. *Quatern. Res.*, **17**, 105–119.

- Brunt, R.L., Di Celma, C.N., Hodgson, D.M., Flint, S.S., Kavanagh, J.P. and Van der Merwe, W.C.** (2013a) Driving a channel through a levee when the levee is high: An outcrop example of submarine down-dip entrenchment. *Mar. Petrol. Geol.*, **41**, 134–145.
- Brunt, R.L., Hodgson, D.M., Flint, S.S., Pringle, J.K., Di Celma, C.N., Prélat, A. and Grecula, M.** (2013b) Confined to unconfined: Anatomy of a base of slope succession, Karoo Basin, South Africa. *Mar. Petrol. Geol.*, **41**, 206–221.
- Campbell, C.V.** (1967) Lamina, laminaset, bed and bedset. *Sedimentology*, **8**, 7–26.
- Cartigny, M.J.B., Ventra, D., Postma, G. and Den Berg, J.H.** (2014) Morphodynamics and sedimentary structures of bedforms under supercritical-flow conditions: New insights from flume experiments. *Sedimentology*, **61**, 712–748.
- de Castro, S., Hernández-Molina, F.J., Rodríguez-Tovar, F.J., Llave, E., Ng, Z.L., Nishida, N. and Mena, A.** (2020) Contourites and bottom current reworked sands: Bed facies model and implications. *Mar. Geol.*, **428**, 106267.
- de Castro, S., Hernández-Molina, F.J., Weger, W., Jiménez-Espejo, F.J., Rodríguez-Tovar, F.J., Mena, A., Llave, E. and Sierro, F.J.** (2021) Contourite characterization and its discrimination from other deep-water deposits in the Gulf of Cadiz contourite depositional system. *Sedimentology*, **68**, 987–1027.
- Cornard, P.H. and Pickering, K.T.** (2019) Supercritical-flow deposits and their distribution in a submarine channel system, Middle Eocene, Ainsa Basin, Spanish Pyrenees. *J. Sed. Res.*, **89**, 576–597.
- Di Celma, C.N., Brunt, R.L., Hodgson, D., Flint, S.S. and Kavanagh, J.P.** (2011) Spatial and temporal evolution of a Permian submarine slope channel–levee system, Karoo Basin, South Africa. *J. Sed. Res.*, **81**, 579–599.
- Dou, L., Best, J.L., Bao, Z., Hou, J., Zhang, L. and Liu, Y.** (2021) The sedimentary architecture of hyperpycnites produced by transient turbulent flows in a shallow lacustrine environment. *Sed. Geol.*, **411**, 105804.
- Dumas, S. and Arnott, R.W.C.** (2006) Origin of hummocky and swaley cross-stratification—The controlling influence of unidirectional current strength and aggradation rate. *Geology*, **34**, 1073–1076.
- Dumas, S., Arnott, R.W.C. and Southard, J.B.** (2005) Experiments on oscillatory-flow and combined-flow bedforms: Implications for interpreting parts of the shallow-marine sedimentary record. *J. Sed. Res.*, **75**, 501–513.
- Fedele, J.J., Hoyal, D., Barnaal, Z., Tulenko, J. and Awalt, S.** (2016) Bedforms created by gravity flows. In: *Autogenic Dynamics and Self-Organization in Sedimentary Systems* (Eds Budd, D.A., Hajek, E.A. and Purkis, S.J.), *SEPM Spec. Publ.*, **106**, 95–121.
- Figueiredo, J.J.P., Hodgson, D.M., Flint, S.S. and Kavanagh, J.P.** (2013) Architecture of a channel complex formed and filled during long-term degradation and entrenchment on the upper submarine slope, Unit F, Fort Brown Fm., SW Karoo Basin, South Africa. *Mar. Petrol. Geol.*, **41**, 104–116.
- Fisher, R.V.** (1983) Flow transformations in sediment gravity flows. *Geology*, **11**, 273–274.
- Flint, S.S., Hodgson, D.M., Sprague, A.R., Brunt, R.L., Van der Merwe, W.C., Figueiredo, J., Prélat, A., Box, D., Di Celma, C. and Kavanagh, J.P.** (2011) Depositional architecture and sequence stratigraphy of the Karoo basin floor to shelf edge succession, Laingsburg depocentre, South Africa. *Mar. Petrol. Geol.*, **28**, 658–674.
- Fuhrmann, A., Kane, I.A., Clare, M.A., Ferguson, R.A., Schomacker, E., Bonamini, E. and Contreras, F.A.** (2020) Hybrid turbidite-drift channel complexes: An integrated multiscale model. *Geology*, **48**, 562–568.
- Fuhrmann, A., Kane, I.A., Schomacker, E., Clare, M.A. and Pontén, A.** (2022) Bottom current modification of turbidite lobe complexes. *Front. Earth Sci.*, **9**, 752066.
- Gallicchio, S., Cerone, D. and Tinterri, R.** (2023) Depositional record of confined turbidites in syn-subduction intraslope basin: insight from the Tufiti di Tusa Formation (Southern Apennines, Italy). *Mar. Petrol. Geol.*, **147**, 105969.
- Gardner, W.D.** (1989) Periodic resuspension in Baltimore canyon by focusing of internal waves. *J. Geophys. Res.*, **94**, 18185–18194.
- Gardner, W.D., Jo Richardson, M., Mishonov, A.V. and Biscaye, P.E.** (2018) Global comparison of benthic nepheloid layers based on 52 years of nephelometer and transmissometer measurements. *Prog. Oceanogr.*, **168**, 100–111.
- Grecula, M., Flint, S., Potts, G., Wickens, D. and Johnson, S.** (2003) Partial ponding of turbidite systems in a basin with subtle growth-fold topography: Laingsburg-Karoo, South Africa. *J. Sed. Res.*, **73**, 603–620.
- Hage, S., Cartigny, M.J.B., Clare, M.A., Sumner, E., Vendettuoli, D., Clarke, J., Hubbard, S., Talling, P., Lintern, D., Stacey, C., Englert, R., Vardy, M., Hunt, J., Yokokawa, M., Parsons, D., Hizzett, J., Azpiroz-Zabala, M. and Vellinga, A.** (2018) How to recognize crescentic bedforms formed by supercritical turbidity currents in the geologic record: Insights from active submarine channels. *Geology*, **46**, 563–566.
- Hansen, L., Callow, R.H.T., Kane, I.A., Gamberi, F., Rovere, M., Cronin, B.T. and Kneller, B.C.** (2015) Genesis and character of thin-bedded turbidites associated with submarine channels. *Mar. Petrol. Geol.*, **67**, 852–879.
- Harms, J.C.** (1969) Hydraulic significance of some sand ripples. *GSA Bulletin*, **80**, 363–396.
- Harms, J.C., Southard, J.B., Spearing, D.R. and Walker, R.G.** (1975) Depositional environments as interpreted from primary sedimentary structures and stratification sequences. *Soc. Sediment. Geol. SEPM Short Course*, **2**, 161.
- Haughton, P.D.W.** (1994) Deposits of deflected and ponded turbidity currents, Sorbas Basin, Southeast Spain. *J. Sed. Res.*, **64**, 233–246.
- Haughton, P.D.W., Barker, S.P. and McCaffrey, W.D.** (2003) ‘Linked’ debrites in sand-rich turbidite systems—Origin and significance. *Sedimentology*, **50**, 459–482.
- Haughton, P.D.W., Davis, C., McCaffrey, W. and Barker, S.** (2009) Hybrid sediment gravity flow deposits – Classification, origin and significance. *Mar. Petrol. Geol.*, **26**, 1900–1918.
- Hiscott, R.N., Hall, F.R. and Pirmez, C.** (1997) Turbidity-current overspill from the Amazon channel: Texture of the silt/ sand load, paleoflow from anisotropy of magnetic susceptibility and implications for flow processes. *Proc Ocean Drilling Prog. Scientific Res.*, **155**, 53–78.
- Hodgson, D.M.** (2009) Distribution and origin of hybrid beds in sand-rich submarine fans of the Tanqua depocentre, Karoo Basin, South Africa. *Mar. Petrol. Geol.*, **26**, 1940–1956.
- Hodgson, D.M., Di Celma, C.N., Brunt, R.L. and Flint, S.S.** (2011) Submarine slope degradation and aggradation and the stratigraphic evolution of channel–levee systems. *J. Geol. Soc. London*, **168**, 625–628.
- Hodgson, D.M., Kane, I.A., Flint, S.S., Brunt, R.L. and Ortiz-Karppf, A.** (2016) Time-transgressive confinement on the

- slope and the progradation of basin-floor fans: Implications for the sequence stratigraphy of deep-water deposits. *J. Sed. Res.*, **86**, 73–86.
- Hodgson, D.M., Peakall, J. and Maier, K.L.** (2022) Submarine channel mouth settings: processes, geomorphology, and deposits. *Front. Earth Sci.*, **10**, 790320.
- Hofstra, M., Peakall, J., Hodgson, D.M. and Stevenson, C.J.** (2018) Architecture and morphodynamics of subcritical sediment waves in an ancient channel-lobe transition zone. *Sedimentology*, **65**, 2339–2367.
- Howlett, D.M., Ge, Z., Nemeč, W., Gawthorpe, R.L., Rotevatn, A. and Jackson, C.A.L.** (2019) Response of unconfined turbidity current to deep-water fold and thrust belt topography: Orthogonal incidence on solitary and segmented folds. *Sedimentology*, **66**, 2425–2454.
- Jelby, M.E., Grundvåg, S.-A., Helland-Hansen, W., Olaussen, S. and Stemmerik, L.** (2020) Tempestite facies variability and storm-depositional processes across a wide ramp: Towards a polygenetic model for hummocky cross-stratification. *Sedimentology*, **67**, 742–781.
- Jobe, Z.R., Lowe, D.R. and Morris, W.R.** (2012) Climbing-ripple successions in turbidite systems: Depositional environments, sedimentation rates and accumulation times. *Sedimentology*, **59**, 867–898.
- Johnson, M.R., van Vuuren, C.J., Visser, J.N.J., Cole, D.L., Wickens, H.d.V., Christie, A.D.M., Roberts, D.L. and Brandl, G.** (2006) Sedimentary rocks of the Karoo Supergroup. In: *The Geology of South Africa* (Eds Johnson, M.R. and Anhaeusser, T.C.R.), pp. 461–499. Geological Society of South Africa and Council for Geoscience, Johannesburg.
- Jones, G.E.D., Hodgson, D.M. and Flint, S.S.** (2015) Lateral variability in clinoform trajectory, process regime, and sediment dispersal patterns beyond the shelf-edge rollover in exhumed basin margin-scale clinoforms. *Basin Res.*, **27**, 657–680.
- Jopling, A.V. and Walker, R.G.** (1968) Morphology and origin of ripple-drift cross-lamination, with examples from the Pleistocene of Massachusetts. *J. Sed. Res.*, **38**, 971–984.
- Kane, I.A. and Hodgson, D.** (2011) Sedimentological criteria to differentiate submarine channel levee subenvironments: exhumed examples from the Rosario Fm. (Upper Cretaceous) of Baja California, Mexico, and the Laingsburg Fm. (Permian), Karoo Basin, South Africa. *Mar. Petrol. Geol.*, **28**, 807–823.
- Kane, I.A. and Pontén, A.S.M.** (2012) Submarine transitional flow deposits in the Paleogene Gulf of Mexico. *Geology*, **40**, 1119–1122.
- Kane, I.A., Pontén, A.S.M., Vangdal, B., Eggenhuisen, J.T., Hodgson, D.M. and Spychala, Y.T.** (2017) The stratigraphic record and processes of turbidity current transformation across deep-marine lobes. *Sedimentology*, **64**, 1236–1273.
- Kneller, B.** (1995) Beyond the turbidite paradigm: physical models for deposition of turbidites and their implications for reservoir prediction. In: *Characterisation of Deep Marine Clastic Systems* (Eds Hartley, A. and Prosser, D.J.), *Geol. Soc. London Spec Publ*, **94**, 31–49.
- Kneller, B.** (2003) The influence of flow parameters on turbidite slope channel architecture. *Mar. Petrol. Geol.*, **20**, 901–910.
- Kneller, B. and Buckee, C.** (2000) The structure and fluid mechanics of turbidity currents: a review of some recent studies and their geological implications. *Sedimentology*, **47**, 62–94.
- Łapcik, P.** (2023) Transitional flow deposits on submarine lobe flank (Veřovice and Lhoty Fms, Albian – Cenomanian, Polish Outer Carpathians). *Sed. Geol.*, **445**, 106329.
- Lowe, D.R.** (1982) Sediment gravity flows; II, Depositional models with special reference to the deposits of high-density turbidity currents. *J. Sed. Res.*, **52**, 279–297.
- Lowe, D.R. and Guy, M.** (2000) Slurry-flow deposits in the Britannia Formation (Lower Cretaceous), North Sea: a new perspective on the turbidity current and debris flow problem. *Sedimentology*, **47**, 31–70.
- Maier, K.L., Rosenberger, K.J., Paull, C.K., Gwiazda, R., Gales, J., Lorenson, T., Barry, J.P., Talling, P.J., McGann, M., Xu, J., Lundsten, E., Anderson, K., Litvin, S.Y., Parsons, D.R., Clare, M.A., Simmons, S.M., Sumner, E.J. and Cartigny, M.J.B.** (2019) Sediment and organic carbon transport and deposition driven by internal tides along Monterey Canyon, offshore California. *Deep Sea Res. Part 1*, **153**, 103108.
- Malarkey, J., Baas, J.H., Hope, J.A., Aspden, R.J., Parsons, D.R., Peakall, J., Paterson, D.M., Schindler, R.J., Ye, L., Lichtman, I.D., Bass, S.J., Davies, A.G., Manning, A.J. and Thorne, P.D.** (2015) The pervasive role of biological cohesion in bedform development. *Nat. Commun.*, **6**, 6257.
- McAnally, W.H., Friedrichs, C., Hamilton, D., Hayter, E., Shrestha, P., Rodriguez, H., Sheremet, A. and Teeter, A.** (2007) Management of fluid mud in estuaries, bays, and lakes. I: Present state of understanding on character and behavior. *J. Hydraul. Eng.*, **133**, 9–22.
- McCave, I.N., Manighetti, B. and Robinson, S.G.** (1995) Sortable silt and fine sediment size/composition slicing: Parameters for palaeocurrent speed and palaeoceanography. *Paleoceanography*, **10**, 593–610.
- McLean, S.R. and Smith, J.D.** (1979) Turbulence measurements in the boundary layer over a sand wave field. *J. Geo. Phys. Res.*, **84**, 7791–7808.
- Miramontes, E., Penven, P., Fierens, R., Droz, L., Toucanne, S., Jorry, S.J., Jouet, G., Pastor, L., Silva Jacinto, R., Gaillot, A., Giraudeau, J. and Raïsson, F.** (2019) The influence of bottom currents on the Zambezi Valley morphology (Mozambique Channel, SW Indian Ocean): In situ current observations and hydrodynamic modelling. *Mar. Geol.*, **410**, 42–55.
- Miramontes, E., Eggenhuisen, J.T., Jacinto, R.S., Poneti, G., Pohl, F., Normandeau, A., Campbell, D.C. and Hernández-Molina, F.J.** (2020) Channel-levee evolution in combined contour current–turbidity current flows from flume-tank experiments. *Geology*, **48**, 353–357.
- Morris, E.A.** (2014) *Stratigraphic Record of Sedimentary Processes in Submarine Channel-Levee Systems*. PhD thesis. University of Liverpool, Liverpool.
- Morris, E.A., Hodgson, D.M., Brunt, R.L. and Flint, S.S.** (2014a) Origin, evolution and anatomy of silt-prone submarine external levées. *Sedimentology*, **61**, 1734–1763.
- Morris, E.A., Hodgson, D.M., Flint, S.S., Brunt, R.L., Butterworth, P.J. and Verhaeghe, J.** (2014b) Sedimentology, stratigraphic architecture, and depositional context of submarine frontal-lobe complexes. *J. Sed. Res.*, **84**, 763–780.
- Morris, E.A., Hodgson, D.M., Flint, S.S., Brunt, R.L., Luthi, S.M. and Kolenberg, Y.** (2016) Integrating outcrop and subsurface data to assess the temporal evolution of a submarine channel-levee system. *AAPG Bulletin*, **11**, 1663–1691.
- Mutti, E.** (1992) *Turbidite sandstones*, p. 275. San Donato, Milan.
- Mutti, E. and Normark, W.R.** (1987) Comparing examples of modern and ancient turbidite systems: Problems and

- concepts. In: *Marine Clastic Sedimentology: Concepts and Case Studies* (Eds Leggett, J.K. and Zuffa, G.G.), pp. 1–38. Graham and Trotman, London.
- Mutti, E. and Normark, W.R.** (1991) An integrated approach to the study of turbidite systems. In: *Seismic Facies and Sedimentary Processes of Submarine Fans and Turbidite Systems* (Eds Weimer, P. and Link, M.H.), pp. 75–106. Springer-Verlag, New York, NY.
- Patacci, M., Houghton, P.D.W. and McCaffrey, W.D.** (2015) Flow behaviour of ponded turbidity currents. *J. Sed. Res.*, **85**, 885–902.
- Peakall, J., McCaffrey, B. and Kneller, B.** (2000a) A process model for the evolution, morphology, and architecture of sinuous submarine channels. *J. Sed. Res.*, **70**, 434–448.
- Peakall, J.D., McCaffrey, W.D., Kneller, B.C., Stelling, C.E., McHargue, T.R. and Schweller, W.J.** (2000b) A process model for the evolution of submarine fan channels: Implications for sedimentary architecture. In: *Fine-Grained Turbidite Systems* (Eds Bouma, A.H. and Stone, C.G.), pp. 73–88. AAPG Memoir 72/SEPM Special Publication 68, Tulsa, Oklahoma.
- Pickering, K.T. and Hiscott, R.N.** (1985) Contained (reflected) turbidity currents from the Middle Ordovician Cloridorme Formation, Quebec, Canada: an alternative to the antidune hypothesis. *Sedimentology*, **32**, 373–394.
- Pierce, C.S., Houghton, P.D.W., Shannon, P.M., Pulham, A.J., Barker, S.P. and Martinsen, O.J.** (2018) Variable character and diverse origin of hybrid event beds in a sandy submarine fan system, Pennsylvanian Ross Sandstone Formation, western Ireland. *Sedimentology*, **65**, 952–992.
- Piper, D.J.W. and Normark, W.R.** (1983) Turbidite depositional patterns and flow characteristics, Navy Submarine Fan, California Borderland. *Sedimentology*, **30**, 681–694.
- Pirmez, C. and Imran, J.** (2003) Reconstruction of turbidity currents in Amazon Channel. *Mar. Petrol. Geol.*, **20**, 823–849.
- Postma, G. and Kleverlaan, K.** (2018) Supercritical flows and their control on the architecture and facies of small-radius sand-rich fan lobes. *Sed. Geol.*, **364**, 53–70.
- Poyatos-Moré, M., Jones, G.D., Brunt, R.L., Hodgson, D.M., Wild, R.J. and Flint, S.S.** (2016) Mud-dominated basin-margin progradation; processes and implications. *J. Sed. Res.*, **86**, 863–878.
- Poyatos-Moré, M., Jones, G.D., Brunt, R.L., Tek, D.E., Hodgson, D.M. and Flint, S.S.** (2019) Clinoform architecture and along-strike facies variability through an exhumed erosional to accretionary basin margin transition. *Basin Res.*, **31**, 920–947.
- Prave, A.R. and Duke, W.L.** (1990) Small-scale hummocky cross-stratification in turbidites: a form of antidune stratification? *Sedimentology*, **37**, 531–539.
- Prélat, A., Hodgson, D.M. and Flint, S.S.** (2009) Evolution, architecture and hierarchy of distributary deep-water deposits: a high-resolution outcrop investigation from the Permian Karoo Basin, South Africa. *Sedimentology*, **56**, 2132–2154.
- Privat, A.M.L.J., Hodgson, D.M., Jackson, C.A.L., Schwarz, E. and Peakall, J.** (2021) Evolution from syn-rift carbonates to early post-rift deep-marine intraslope lobes: The role of rift basin physiography on sedimentation patterns. *Sedimentology*, **68**, 2563–2605.
- Pysklywec, R.N. and Mitrovica, J.X.** (1999) The role of subduction-induced subsidence in the evolution of the Karoo Basin. *J. Geol.*, **107**, 155–164.
- Rebesco, M., Hernández-Molina, F.J., Van Rooij, D. and Wåhlin, A.** (2014) Contourites and associated sediments controlled by deep-water circulation processes: State-of-the-art and future considerations. *Mar. Geol.*, **352**, 111–154.
- Rodrigues, S., Hernández-Molina, F.J., Hillenbrand, C.D., Lucchi, R.G., Rodríguez-Tovar, F.J., Rebesco, M. and Larter, R.D.** (2022) Recognizing key sedimentary facies and their distribution in mixed turbidite–contourite depositional systems: The case of the Pacific margin of the Antarctic Peninsula. *Sedimentology*, **69**, 1953–1991.
- Sanders, J.E.** (1965) Primary sedimentary structures formed by turbidity currents and related re-sedimentation mechanisms. In: *Primary Sedimentary Structures and their Hydrodynamic Interpretation* (Ed. Middleton, G.V.), *SEPM Special Publication*, **12**, 192–219.
- Schindler, R.J., Parsons, D.R., Ye, L., Hope, J.A., Baas, J.H., Peakall, J., Manning, A.J., Aspden, R.J., Malarkey, J., Simmons, S., Paterson, D.M., Lichtman, I.D., Davies, A.G., Thorne, P.D. and Bass, S.J.** (2015) Sticky stuff: Redefining bedform prediction in modern and ancient environments. *Geology*, **43**, 399–402.
- Shanmugam, G., Spalding, T.D. and Rofheart, D.H.** (1993a) Process sedimentology and reservoir quality of deep-marine bottom-current reworked sands (sandy contourites): An example from the Gulf of Mexico. *AAPG Bulletin*, **77**, 1241–1259.
- Shanmugam, G., Spalding, T.D. and Rofheart, D.H.** (1993b) Traction structures in deep-marine, bottom-current-reworked sands in the Pliocene and Pleistocene, Gulf of Mexico. *Geology*, **21**, 929–932.
- Sixsmith, P.J., Flint, S.S., Wickens, H.D. and Johnson, S.D.** (2004) Anatomy and stratigraphic development of a basin floor turbidite system in the Laingsburg Formation, Main Karoo Basin, South Africa. *J. Sed. Res.*, **74**, 239–254.
- Slootman, A. and Cartigny, M.J.B.** (2020) Cyclic steps: Review and aggradation-based classification. *Earth Sci. Rev.*, **201**, 102949.
- Smith, R.M.H.** (1990) A review of stratigraphy and sedimentary environments of the Karoo Basin of South Africa. *J. Afr. Earth Sci.*, **10**, 117–137.
- Sorby, H.C.** (1908) On the application of quantitative methods to the study of the structure and history of rocks. *Q. J. Geol. Soc. Lond.*, **64**, 171–233.
- Southard, J.B.** (1991) Experimental determination of bed-form stability. *Annu. Rev. Earth Planet. Sci.*, **19**, 423–455.
- Southard, J.B. and Boguchwal, L.A.** (1990) Bed configuration in steady unidirectional water flows; Part 2, Synthesis of flume data. *J. Sed. Res.*, **60**, 658–679.
- Spychala, Y.T., Hodgson, D.M., Flint, S.S. and Mountney, N.P.** (2015) Constraining the sedimentology and stratigraphy of submarine intraslope lobe deposits using exhumed examples from the Karoo Basin, South Africa. *Sed. Geol.*, **322**, 67–81.
- Spychala, Y.T., Eggenhuisen, J.T., Tilston, M. and Pohl, F.** (2020) The influence of basin setting and turbidity current properties on the dimensions of submarine lobe elements. *Sedimentology*, **67**, 3471–3491.
- Stevenson, C.J., Peakall, J., Hodgson, D.M., Bell, D. and Privat, A.** (2020) T_B or not T_B : banding in turbidite sandstones. *J. Sed. Res.*, **90**, 821–842.
- Stow, D.A.V. and Johansson, M.** (2000) Deep-water massive sands: Nature, origin and hydrocarbon implications. *Mar. Petrol. Geol.*, **17**, 145–174.

- Stow, D.A.V. and Lovell, J.P.B.** (1979) Contourites: their recognition in modern and ancient sediments. *Earth Sci. Rev.*, **14**, 251–291.
- Stow, D.A.V. and Shanmugam, G.** (1980) Sequence of structures in fine-grained turbidites: Comparison of recent deep-sea and ancient flysch sediments. *Sed. Geol.*, **25**, 23–42.
- Stow, D.A.V. and Smillie, Z.** (2020) Distinguishing between deep-water sediment facies: Turbidites, contourites and hemipelagites. *Geosciences*, **10**, 68.
- Sumner, E.J., Amy, L.A. and Talling, P.J.** (2008) Deposit structure and processes of sand deposition from decelerating sediment suspensions. *J. Sed. Res.*, **78**, 529–547.
- Sumner, E.J., Talling, P.J. and Amy, L.A.** (2009) Deposits of flows transitional between turbidity current and debris flow. *Geology*, **37**, 991–994.
- Talling, P.J., Amy, L.A., Wynn, R.B., Peakall, J. and Robinson, M.** (2004) Beds comprising debrite sandwiched within co-genetic turbidite: origin and widespread occurrence in distal depositional environments. *Sedimentology*, **51**, 163–194.
- Talling, P.J., Masson, D.G., Sumner, E.J. and Malgesini, G.** (2012) Subaqueous sediment density flows: depositional processes and deposit types. *Sedimentology*, **59**, 1937–2003.
- Tankard, A., Welsink, H., Aukes, P., Newton, R. and Stettler, E.** (2009) Tectonic evolution of the Cape and Karoo basins of South Africa. *Mar. Petrol. Geol.*, **26**, 1379–1412.
- Tankard, A., Welsink, H., Aukes, P., Newton, R. and Stettler, E.** (2012) Geodynamic interpretation of the Cape and Karoo basins, South Africa. In: *Regional Geology and Tectonics: Phanerozoic Passive Margins, Cratonic Basins and Global Tectonic Maps* (Eds Roberts, D.G. and Bally, A.W.), pp. 868–945. Elsevier B.V., Amsterdam.
- Tinterri, R.** (2011) Combined flow sedimentary structures and the genetic link between sigmoidal- and hummocky-cross stratification. *GeoActa*, **10**, 43–85.
- Tinterri, R. and Muzzi Magalhaes, P.M.** (2011) Synsedimentary structural control on foredeep turbidites: An example from Miocene Marnoso-arenacea Formation, Northern Apennines, Italy. *Mar. Petrol. Geol.*, **28**, 629–657.
- Tinterri, R., Mazza, T. and Magalhaes, P.M.** (2022) Contained-reflected megaturbidites of the Marnoso-arenacea Formation (Contessa Key Bed) and Helminthoid Flysches (Northern Apennines, Italy) and Hecho Group (South-Western Pyrenees). *Front. Earth Sci.*, **10**, 817012.
- Van der Merwe, W.C., Hodgson, D.M. and Flint, S.S.** (2009) Widespread syn-sedimentary deformation on a muddy deep-water basin-floor: the Vischkuil Formation (Permian), Karoo Basin, South Africa. *Basin Res.*, **21**, 389–406.
- Van der Merwe, W.C., Hodgson, D.M., Brunt, R.L. and Flint, S.S.** (2014) Depositional architecture of sand-attached and sand-detached channel-lobe transition zones on an exhumed stepped slope mapped over a 2500 km² area. *Geosphere*, **10**, 1076–1093.
- Walker, R.C.** (1967) Turbidite sedimentary structures and their relationship to proximal and distal depositional environments. *J. Sed. Petrol.*, **37**, 25–43.
- Wang, Z. and Plate, E.C.H.J.** (1996) A preliminary study on the turbulence structure of flows of non Newtonian fluid. *J. Hydraul. Res.*, **34**, 345–361.
- de Weger, W., Hernández-Molina, F.J., Flecker, R., Sierro, F.J., Chiarella, D., Krijgsman, W. and Manar, M.A.** (2020) Late Miocene contourite channel system reveals intermittent overflow behavior. *Geology*, **48**, 1194–1199.
- Wilson, I.G.** (1972) Aeolian bedforms - Their development and origins. *Sedimentology*, **19**, 173–210.
- Winterwerp, J.C. and van Kesteren, W.G.M.** (2004) Flocculation processes. In: *Introduction to the Physics of Cohesive Sediment in the Marine Environment* (Eds Winterwerp, J.C. and van Kesteren, W.G.M.), pp. 87–119. Elsevier, Amsterdam.
- Yokokawa, M., Masuda, F. and Endo, N.** (1995) Sand particle movement on migrating combined-flow ripples. *J. Sed. Res.*, **65**, 40–44.
- Zhao, Y., Liu, Z., Zhang, Y., Li, J., Wang, M., Wang, W. and Xu, J.** (2015) In situ observation of contour currents in the northern South China Sea: Applications for deepwater sediment transport. *Earth Planet. Sci. Lett.*, **430**, 477–485.

Manuscript received 17 July 2023; revision accepted 20 December 2023